Precambrian Research 409 (2024) 107453

Contents lists available at ScienceDirect

Precambrian Research

journal homepage: www.elsevier.com/locate/precamres

Hydrothermal seawater eutrophication triggered local macrobiological experimentation in the 2100 Ma Paleoproterozoic Francevillian sub-basin

Ernest Chi Fru [a,*], Jérémie Aubineau [b,c], Olabode Bankole [c], Mohamed Ghnahalla [c], Landry Soh Tamehe [d], Abderrazak El Albani [c]

[a] College of Physical and Engineering Sciences, School of Earth and Ocean Sciences, Centre for Geobiology and Geochemistry, Cardiff University, Cardiff CF10 3AT, Wales, UK
[b] Géosciences Environnement Toulouse, CNRS UMR 5563 (CNRS/UPS/IRD/CNES), Université de Toulouse, Observatoire Midi-Pyrénées, Toulouse, France
[c] Université de Poitiers UMR 7285-CNRS, Institut de Chimie des Milieux et Matériaux de Poitiers, 5, rue Albert Turpin (Bât B35), 86073 Poitiers Cedex, France
[d] China Nonferrous Metals (Guilin) Geology and Mining Co. Ltd, Guilin 541004, China

ARTICLE INFO

Keywords:
Manganese carbonates
Iron carbonates
Proterozoic
Congo Craton
Seawater oxygenation

ABSTRACT

It is thought that the global predominance of small-size unicellular prokaryotic life in the oceans until the emergence of large-size multicellular organisms to ecological dominance in the Ediacaran Ocean after 635 million years ago (Ma), was partly constrained by paleo-dynamic nutrient limitation, with phosphorus (P) being the principal limiting resource. Here we couple an episode of intense submarine hydrothermal alteration of a nutrient-rich seafloor reservoir to the collision of the Congo-São Francisco cratons at ~2100 Ma, to unravel a paleo-geodynamic incident of seawater P enrichment in the Paleoproterozoic Francevillian sub-basin. We propose that this previously unrecognized local pulse in dissolved seawater P concentration, of comparable magnitude to Ediacaran seawater levels, set the stage for Earth's earliest biospheric experimentation towards macrobiological complexity ~2100 million years ago.

1. Introduction

Being a critical biolimiting nutrient over geological timescales (Tyrrell, 1998), low seawater phosphorus (P) concentration is frequently advanced as a key cause of mildly productive Proterozoic oceans, reduced organic carbon (C_{org}) burial rates and limited ocean–atmosphere oxygenation (e.g., Reinhard et al., 2017; Guilbaud et al., 2020; Laakso et al., 2020; Poulton et al., 2021; Alcott et al., 2022; Chi Fru et al., 2023; Dodd et al., 2023). This view is anchored on the significance of P being the backbone of nucleic acids, cell membrane phospholipids and cell energy trafficking by adenosine triphosphate (ATP).

Thus, environmental phosphate (PO_4^{3-}) bioavailability is thought to have exerted considerable influence on the pace of biological evolution from small unicellular life forms to large multicellular metazoans (e.g., Brocks et al., 2017; Reinhard et al., 2017, 2020; Eckford-Soper et al., 2022). Further, the dependence of life on oxidoreductase enzymes containing reactive metal cores to generate cellular energy (Jelen et al., 2016; Dupont et al., 2006, 2010; Moore et al., 2017), has spawned the hypothesis that fluctuations in trace metal abundance through Earth history masterminded their selective use in enzymatic reactions through time (Saito et al., 2003; Dupont et al., 2006, 2010; Robbins et al., 2013; Scott et al., 2013; Moore et al., 2017).

According to conventional thinking, unequivocal evidence for eukaryotic fossils first appeared in the geological record some 1700–1600 million years ago (Ma), almost a billion years before the appearance of animals after 635 Ma (Knoll et al., 2006; Javaux, 2011; Buffield, 2009, Butterfield, 2015; Zhu et al., 2016; Reinhard et al., 2020; Eckford-Soper et al., 2022). Even more profound, some four hundred millions earlier, the ~2100 Ma Paleoproterozoic Francevillian sub-basin in southeastern Gabon (Fig. 1A), records a unique assemblage of enigmatic macroscopic specimens interpreted by some studies (e.g., El Albani et al., 2010, 2014, 2019, 2023; Ossa Ossa et al., 2023) and disputed by others (e.g., Anderson et al., 2016; Fakhraee et al., 2023), to represent models of Earth's earliest oxygen-respiring colonial life forms, some which were capable of complex motility behaviour. Moreover, persistent association of the Francevillian macrofossils with a rich benthic microbial community (Aubineau et al., 2018, 2019, 2021), is consistent with the requirements for a high energy resource-rich ecosystem to enable evolutionary gigantism and complexity (Ward et al., 2012). Thus, the recent proposition of a macro-eukaryotic lifestyle

---

* Corresponding author.
E-mail address: ChiFruE@Cardiff.ac.uk (E. Chi Fru).

https://doi.org/10.1016/j.precamres.2024.107453
Received 19 January 2024; Received in revised form 24 May 2024; Accepted 25 May 2024
Available online 31 May 2024
0301-9268/© 2024 Elsevier B.V. All rights are reserved, including those for text and data mining, AI training, and similar technologies.

resulting in cellular Zn, Ni and Co enrichment in the Francevillian macrofossils (El Albani et al., 2023; Ossa Ossa et al., 2023) raises the question of whether a shift in environmental nutrient supply to the paleo-Francevillian sub-basin drove the emergence of these enigmatic macrofossils.

In the modern ocean, small phytoplankton and picoeukaryotes dominate low nutrient habitats and larger complex organisms more productive nutrient-rich ecosystems. Similarly, it is thought that ecological dominance of higher eukaryotic algae in post-Cryogenian Snowball PO_4^{3-}-rich seawater powered complex food webs that sustained more efficient nutrient and energy exchange to drive oxygen-dependent Ediacaran ecosystems towards larger and more complex metazoans (Brocks et al., 2017; Van Maldegem et al., 2019). Thus, environmental oxygen concentration increasing to above a certain minimum threshold may likely have been a key contributor to greater macrobiological complexity (e.g., Planavsky et al., 2014; Cole et al., 2020; Reinhard et al., 2020; Eckford-Soper et al., 2022; Craig et al., 2023). Although the link between environmental oxygen threshold

Click here to access/download;Figure;Figure 1.pdf

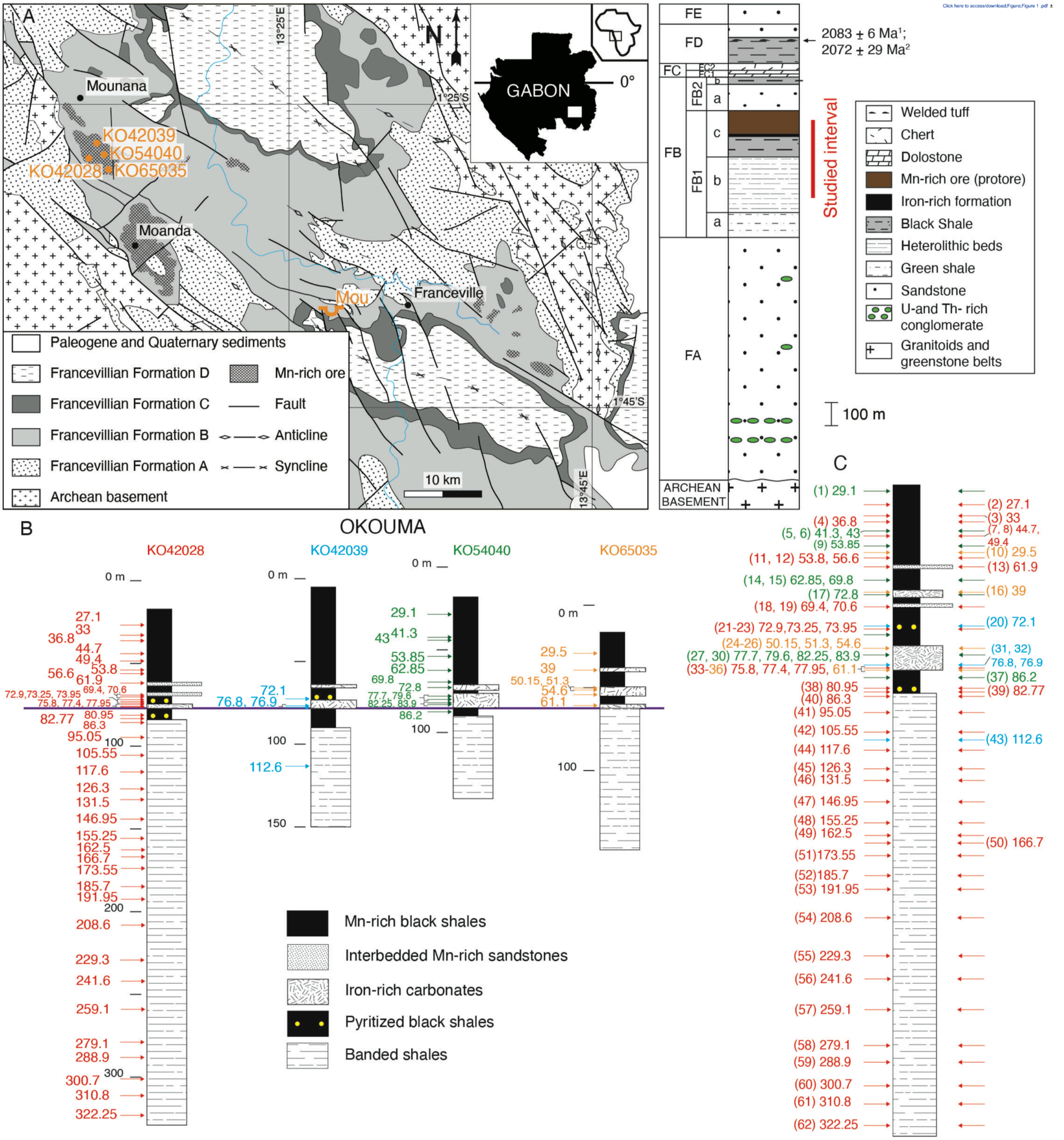

Fig. 1. A) Geological map of the Francevillian Group showing location of the four sampled drill holes (KO42039, KO54040, KO42028 and KO65035). The Bangombe Plateau quarry that records the Francevillian biota is indicated by Mou. B) Lithostratigraphy of individual drill cores. C) Combined generalized drill core stratigraphy. FA to FE represents Franceville A, B, C, D and E Formations. The FB Formation is divided into FB1 and FB2 members composed of FB_{1a}, FB_{1b} and FB_{1c} and FB_{2a} and FB_{2b} units, respectively. The horizontal purple line is the reference datum for horizontalization, as represented by Reynaud et al. (2018), which allowed stratigraphic correlations between drill cores.

levels and the role of genetic innovation in the transition to complex multicellular life is debated (e.g., Buffield, 2009, Erwin et al., 2011; Mills et al., 2014; Bozdag et al., 2021), oxygen availability and genetic innovation, in tandem with nutrient levels, likely worked in synergy to drive biological diversification towards greater complexity, given that low environmental oxygen levels also select for small size individuals and higher levels large size organisms (Sperling et al., 2013).

In line with this view, there is compelling evidence linking a stable shallow oxygenated continental seawater margin setting with emergence of the Francevillian macrofossils (El Albani et al., 2010, 2014). This is intriguing because the Francevillian macrofossils appear on the heels of the 2450–2200 Ma Great Oxidation Event (GOE) (Poulton et al., 2021) as are the Ediacaran macrofossils that coincide with the Neoproterozoic Oxygenation Event (NOE). However, the role of nutrient bioavailability, and particularly PO_4^{3-}, remains to be associated with gigantism in the Francevillian macrofossils. This has resulted in considerable uncertainties on what triggered their emergence and whether their biogenicity can be pinned to environmental conditions that enable macrobiological evolution.

Here we explore the hypothesis that dramatic environmental change resulting in high nutrient bioavailability in seawater drives trophic level complexity and evolutionary gigantism (Ward et al., 2012; Reinhard et al., 2016), to explore the biogenic bridge between environmental change, seawater nutrient bioavailability and the appearance of macroorganisms in the Francevillian sub-basin at ~2100 Ma. To achieve this goal, we undertake a systematic reconstruction of a whole suite of seawater biogeochemical conditions that prevailed just before the Francevillian macrofossils that grew to >17 cm long forms, some as lenticular, segmented, tubular, lobate and string shaped assemblages (El Albani et al., 2010, 2014, 2019, 2023; Ikouanga et al., 2023), emerged.

The biogeochemical evidence surprisingly reveals unprecedented transitory enrichment of the ~2100 Ma Paleoproterozoic Francevillian sub-basin seawater margin with P levels comparable to those that supported the rise of the Ediacaran biota just before the appearance of the Francevillian macrofossils. We track the trigger for this abrupt local environmental change to hydrothermal alteration of a nutrient-rich seafloor reservoir initiated by collision of the Congo-São Francisco cratons during the Eburnean-Transamazonian orogeny.

2. Geological setting

The up to 2.5 km-thick epicontinental sedimentary package of the ~2100 to 2000 Ma Francevillian Group in southeastern Gabon and its exquisitely preserved and unmetamorphosed rocks, comprise five distinct formations emplaced unconformably on an Archean granitoid and greenstone belt basement (Fig. 1A). The ~1000 m-thick basal FA Formation, mainly of fluvial to deltaic sandstones, is rich in organic matter, hematite and uranium.

The overlying FB, FC, FD, FE formations were deposited in predominantly marine environments (Mossmann, et al., 2005; Canfield et al., 2013; Reynaud et al., 2018), with the $FB_{1a\text{-}c}$ and $FB_{2a\text{-}b}$ units dominated by fine-grained shales containing a Mn-rich ore (protore) made up of Mn-rich carbonates underlain by a thin Mn-rich sandstone layer and an Fe-rich formation (Fig. 1A) composed mainly of Fe-rich carbonates (Canfield et al., 2013; Ngombi Pemba et al., 2014; Reynaud et al., 2018). The FB1b unit comprising heterolithic beds (banded shales), together with the Fe-Mn-rich lithologies of the FB1c unit, constitute the lithologies analysed in this study (Fig. 1A).

The FB_2 Member hosts the macrofossils, which are associated with numerous microbial mat-related structures (Aubineau et al., 2018; El Albani et al., 2010, 2014, 2019; Reynaud et al., 2018), while Mn deposition in the upper FB_1 Member is believed to correlate temporally with deposits in the São Francisco Basin, Brazil, at the time amalgamated to the Francevillian Group (dos Santos et al., 2023). Correlation of $\delta^{13}C_{carb}$ and $\delta^{13}C_{org}$ in the FB and lower FC formations with the Zaonega Formation, Russia, together with geochronology, constrain the depositional age of the Francevillian Group to ~2.11–2.06 Ga. (Bros et al., 1992; Thiéblemont et al., 2009; Kump et al., 2011; Canfield et al., 2013; Sawaki et al., 2017).

3. Materials and methods

3.1. Sample collection and preparation

Stratigraphic reconstruction relied on identification of the Fe-rich carbonate facies as a transitional boundary marker from the FB_{1b} to the FB_{1c} unit (Weber, 1968; Gauthier-Lafaye and Weber, 2003; Canfield et al., 2013; Reynaud et al., 2018). The latter studies have extensively described the sedimentological structures and sequence stratigraphic framework of the FB Formation. This well-recognized Fe-rich carbonate facies described in Canfield et al. (2013) enabled correlation between drillholes (KO42028, KO65035, KO54040 and KO42039) obtained from the Okouma Plateau area (Fig. 1B, C). The drillholes intersect various sections, thickness, and depths of the $FB_{1b\text{-}c}$ units (Reynaud et al., 2018), with the deepest KO42028 reaching ~325 m and KO65035, KO54040 and KO42039 ~150, 140 and 150 m, respectively. Four main lithologies common to the drillholes include the 51–240 m thick laminated heterolithic siltstones (banded shales), characterized by creamy-whitish dolomitic bands alternating with siltstones and greyish shales (Figs. 1C, D & 2A-F). These are overlain by 5–10 m thick pyritized shales, and then by an 8–17 m thick Fe-rich carbonate facies, sometimes containing breccias and pyrite laminae. This passes over to a thin pyritized shale unit, overlain by 41–53 m thick Mn-rich black shales with a thin Mn-rich sandstone horizon at the base.

3.2. Petrography and mineralogy

Polished thin sections were prepared for representative samples and examined under a polarized Nikon Eclipse E-600 optical microscope at the University of Poitiers, France. The thin sections were carbon-coated and studied with a JEOL scanning electron microscope (SEM) coupled with energy dispersive X-ray (EDX) for textural, mineralogical and spot elemental composition in backscattered electron (BSE) mode. X-ray diffraction (XRD) on bulk rock and <2 µm clay fractions was conducted with a Bruker D8 ADVANCE diffractometer as previously established by Moore and Reynolds (1997) and Ngombi Pemba et al. (2014).

3.3. Bulk rock geochemistry

Approximately 300 mg of powdered samples were fused with 900 mg ultra-pure lithium metaborate ($LiBO_2$) for trace and major element analyses (Carignan et al., 2001; Ngombi Pemba et al., 2014). Major elements (MEs) were measured with an inductively coupled plasma optical emission spectrometer (ICP-OES) and trace elements (TEs) by ICP mass spectrometry (ICP-MS) at *Service d'Analyse des Roches et Minéraux (SARM)*, Nancy, France. Measurement uncertainties and detection limits are presented in Tables S1 and S2. Analytical procedures were validated with basalt BR, anorthosite AN-G, diorite DR-N, serpentinite UB-N and granite GH as geological reference standards. Selected redox sensitive metals, major elements and TEs were normalized with Al as a detrital indicator and standardized to Post-Archean Australian Shale (PAAS) composition (Taylor and McLennan, 1985) to distinguish authigenic from detrital enrichments. Elemental enrichment factor (EF) was calculated as $EF_X = [(X/Al)_{sample}/(X/Al)_{PAAS}]$, where X = concentration of element of interest (Tribovillard et al., 2006).

3.4. Chemical index of alteration (CIA)

The chemical index of alteration (CIA) was used to quantify the degree of chemical weathering of source rocks, where CIA $= [Al_2O_3/(Al_2O_3 + CaO^{*} + Na_2O + K_2O)] \times 100$, in molar proportions (Fedo and Babechuk, 2023). For the CIA analysis, CaO* represents the quantity

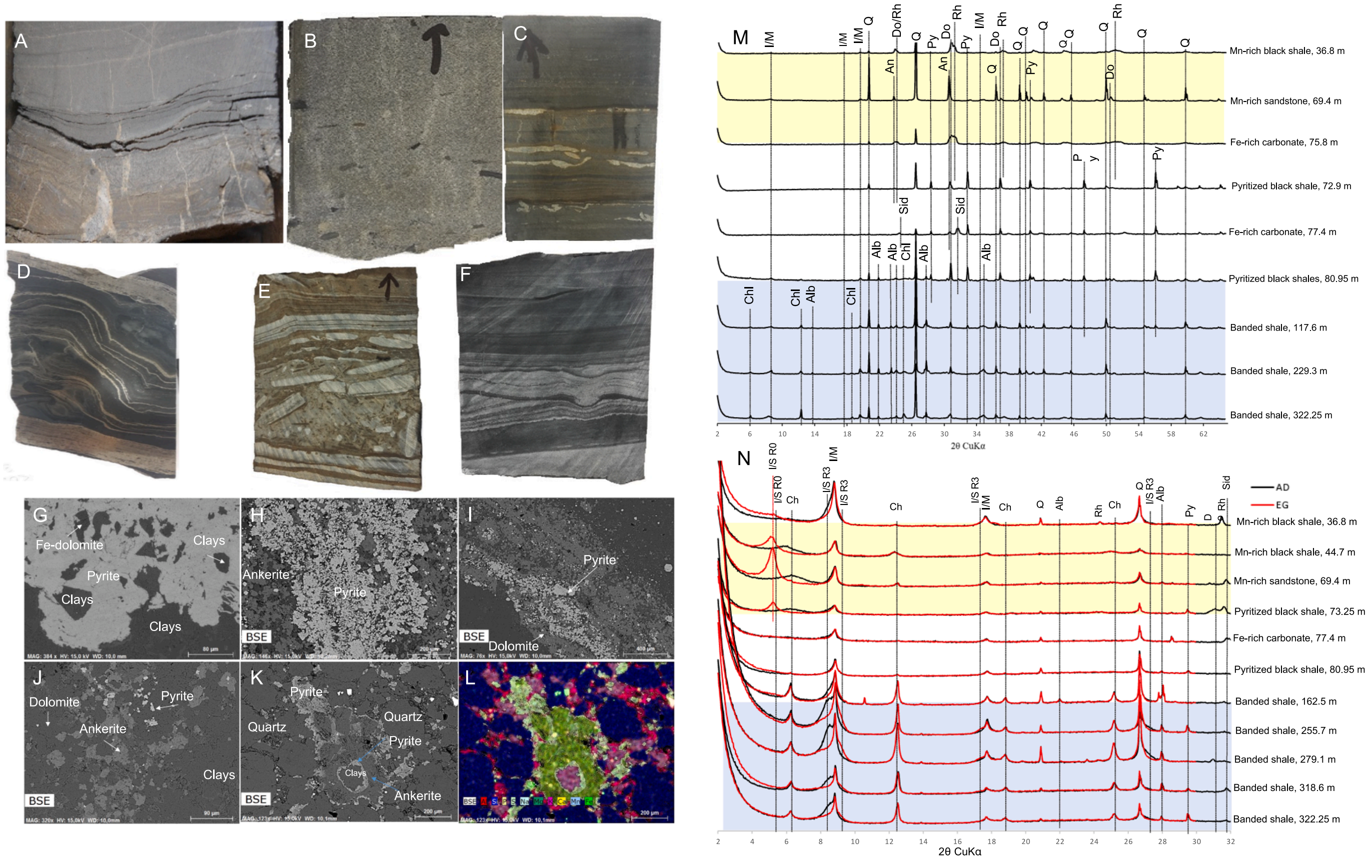

Fig. 2. Lithofacies, petrographic and mineralogical analysis of representative lithologies for the studied section. A) Mn-rich black shale. B) Mn-rich sandstone. C) Pyritized black shale. D) Fe-rich carbonate shales. E) Dolomitic and ankeritic facies showing breccias composed of dolomitic clasts. F) Banded shales showing white bands of silty dolomite alternating with black shale units. G-H) Dispersed pyrite engulfing clays and Fe-dolomite within the Fe-rich carbonate. I-J) Dolomitic and ankeritic minerals in the Mn-rich black shales. K-L) Clay and ankerite minerals filling the matrix of the underlying banded shale. M) Bulk rock X-Ray Diffractograms (XRD) for representative samples. N) XRD spectra for <2 μm clay fraction for representative samples from the Okouma Plateau. Black spectra are for air-dry (AD) samples and red for ethylene–glycol (EG). *Chl, chlorite; I/M, illite/micas; I/S, illite/smectite; Alb, albite; Q, quartz; Py, pyrite; An, ankerite, Do, dolomite; Rh, rhodochrosite. Sid, siderite.*

of CaO associated with silicate phases after correction for CaO-rich phases (McLennan et al., 1993). We assumed moles of silicate CaO* = Na_2O when CaO > Na_2O in molar proportions and CaO* = CaO when CaO ≤ Na_2O in molar proportions (e.g., Jian et al., 2013). Weathering changes and sediment source were further inferred by projecting the obtained CIA values on an Al_2O_3-(CaO* + Na_2O)-K_2O ternary diagram. CIA values >80 depict intense leaching of mobile Ca^{2+}, Na^{+}, K^{+} cations relative to immobile Al^{3+} during chemical weathering of parent rock, while values <50 represent weak to near absence of chemical weathering.

The CIA values of sedimentary rocks can be influenced by input source composition, chemical weathering, sediment recycling, sorting and diagenesis, which can complicate comparisons of sedimentary archives (Fedo et al., 1995; Fedo and Babechuk, 2023). We therefore considered the effects of these processes on our CIA values. The data were interpreted as CIA ≤ 50 % for unweathered igneous rocks, 60–80 % for moderately weathered rocks and >80 % for highly weathered rocks (Fedo et al., 1995; Fedo and Babechuk, 2023).

3.5. *Redox reconstruction*

Rare Earth Elements (REEs), redox sensitive metals, C and N systematics and Fe speciation were combined to assess redox depositional conditions on 58 representative samples, bracketing the $FB1_{b-c}$ units. Iron speciation was performed at Cardiff University, UK, following the refined Fe extraction method of Poulton and Canfield (2005), taking into consideration pitfalls caused by elevated carbonate and low Fe content, as reviewed by Raiswell et al. (2018). Data were compared with previously published results for the correlative Bangombe Plateau (Canfield et al., 2013). Instrument interference on Eu composition caused by Ba was evaluated as described in Fig. S1 and shown to be insignificant.

3.6. *Carbon and nitrogen stable isotope analysis*

Organic carbon ($\delta^{13}C_{org}$) and whole rock $\delta^{15}N_{bulk}$ isotope analyses were performed on the same samples used for Fe-based redox reconstruction. First, powdered samples were treated with 6 N HCl at 70 °C for 1 h to remove carbonate minerals. After repeated washing with distilled water and centrifugation to neutral pH, the residue was dried in a clean hood overnight. Small aliquots of de-carbonated and whole-rock powdered samples were weighed and sealed in tin capsules for C and N isotope analyses, respectively, with a blank inserted between measurements. Data were obtained by flash combustion on a Thermo Scientific DELTA V Advantage isotope ratio mass spectrometer (IRMS), operated under continuous helium flow mode, and coupled to a COSTECH 4010 elemental analyzer, at the University of California, Riverside, USA. The data are reported in delta (δ) notations, as part per mil (‰) deviation relative to Vienna Pee Dee belemnite (VPDB) for carbon and atmospheric N_2 for nitrogen. The $\delta^{13}C_{org}$ and $\delta^{15}N_{bulk}$ data were calibrated against two internal laboratory standards – acetanilide from two different batches ($\delta^{13}C = -27.9$ ‰, $\delta^{15}N = -0.8$ ‰ and $\delta^{13}C = -33.7$ ‰, $\delta^{15}N = -0.8$ ‰) and Hawaiian glycine ($\delta^{13}C = -36.6$ ‰, $\delta^{15}N = 11.3$ ‰)

and two international reference standards, SDO-1 ($\delta^{13}C = -30.0$ ‰, $\delta^{15}N = -0.8$ ‰) and SGR ($\delta^{13}C = -29.3$ ‰, $\delta^{15}N = -17.4$ ‰) (Dennen et al., 2006). Replicate analyses produced a 0.09 ‰ standard deviation (1σ) for $\delta^{13}C_{org}$ (n = 9) and 0.11 ‰ for $\delta^{15}N_{bulk}$ (n = 8). Total organic carbon (TOC) and total nitrogen (TN) concentrations were calculated from peak areas of CO_2 and N_2, respectively. Reported $\delta^{15}N_{bulk}$ values are only for samples with TN concentrations above instrument detection limit.

4. Results

4.1. Lithostratigraphic enrichment of major and trace elements

Consistent with lithostratigraphy (Fig. 2A-F) and mineralogical analyses (Fig. 2G-N), significant enrichment of a range of MEs, TEs and REEs, delineate a sharp transition from the underlying banded shales to the overlying Fe-Mn-rich lithologies (Fig. 3A-P; Tables S3-5). Particularly, considerable P_2O_5 (P) and Fe_2O_3 (Fe) enrichment differentiates the Fe-rich carbonates from the rest of the lithologies (Fig. 3A, M, N). The banded shales are enriched in detrital quartz, albite and chlorite, with illite/mica present to a lesser extent, while the Fe-Mn-rich lithologies containing siderite ($FeCO_3$) and rhodochrosite ($MnCO_3$) as dominant Fe and Mn minerals, respectively (Fig. 2M, N), exhibit negligible detrital incorporation, as are the pyritized black shales. The latter observations are consistent with normalization of TE content with detrital Al and with up sequence switch towards greater chemical weathering CIA values (Figs. 4, 5A & Table S3).

The Al_2O_3 and TiO_2 content show similar co-enrichment trends across the section (Fig. 5B, C). Fe_2O_3 peaks in the Fe-rich carbonates and is within a comparable range in the Mn-rich black shales and banded shales (Fig. 5D). MnO concentrations show a systematic increase up section (Fig. 5E), with corresponding Fe_2O_3/MnO ratios decreasing in a similar direction (Fig. 5F). The ratios of Fe_2O_3/TiO_2 and Fe_2O_3/Al_2O_3 (Fig. 5G, H) display a comparable behaviour as are those of MnO/TiO_2 and MnO/Al_2O_3 ratios (Fig. 5I, J). Considering Al and Ti as a detrital tracer, the Fe_2O_3 content in the Mn-rich black shales and banded shales appears to have experienced greater dilution by detrital input compared to Fe_2O_3 in the Fe-rich carbonates (Fig. 5G, H). Similarly, detrital input is suggested to have exerted a stronger influence on MnO enrichment in the Mn-rich black shales and banded shales than in the Fe-rich carbonates (Fig. 5I, J).

Except for a moderate positive correlation of 54 % for the banded shales, a weak linear correlation of 18 % is observed when Fe_2O_3/TiO_2 ratios for the Mn-rich black shales and Fe-rich carbonates are plotted against Fe_2O_3 concentrations (Fig. 6A)—being up to 71 % linearly correlated cross all three lithologies combined (Fig. 6B). On the other hand, MnO/TiO_2 ratios for the banded shales, Fe-rich carbonates and the Mn-rich black shales lithologies show a strong positive correlation of 96 %, 82 % and 74 %, with MnO concentrations, respectively (Fig. 6C)—being only 47 % linearly correlated for all three compared (Fig. 6D).

4.2. Indicators of hydrothermal activity

The corresponding Fe/Ti versus Al/(Al + Fe + Mn) values for the individual facies indicate that the Fe-rich carbonates were deposited under more influential hydrothermal activity, with one sample plotting in the intense hydrothermal field (Fig. 7A). While both the Mn-rich carbonates and the banded shales show lower Fe/Ti ratios, the latter lithologies are distinguished by extremely high Al/(Al + Fe + Mn) values.

Overall, the samples group with banded iron formations (BIFs) of comparable age and of low temperature hydrothermal origin in the northwestern Congo Craton (Fig. 7B, C). However, cross plots of their $(Sm/Yb)_{CN}$ versus $(Eu/Sm)_{CN}$ ratios (Fig. 7C) indicate subtle geochemical differences consistent with varying degrees of hydrothermal fluid composition and seawater mixtures. Distinctively, four of the Fe-rich carbonates and one each for the pyritized and Mn-rich black shales fall between 0.1–1 % hydrothermal fluid composition and up to 1–5 % for one Fe-rich carbonate sample (Fig. 7C). Although less evident on the Y/Ho versus Eu/Eu* plot (Fig. S2A), hydrothermal fluid contribution to the facies is further indicated by PAAS normalized REE spider diagrams with variable positive Eu anomalies (Fig. 7D-G).

Moving up sequence, the sediments record average Y/Ho ratios of 30.5, 37.1, 33.9 and 36.4 for the banded shales, Fe-rich carbonates, Mn-rich sandstones, and Mn-rich black shales, respectively, and 36.3 for the two pyritized units (Fig. S2A & Table S3). The Fe-carbonates have the lowest ΣREE + Y content, moderate for the Mn-rich lithologies and highest for the banded shales (Fig. S2B & Table S3). These observations highlight a relational increase in total ΣREE + Y with the greater detrital composition of the banded shales and the higher Y/Ho ratios in the Fe-Mn-rich and pyritic sediments in association with a predominantly chemical origin (Fig. S2). The studied section overall shows a typical seawater-like positive shale normalized Y anomaly (Fig. 7D-G).

However, the REE data, together with those of contemporaneous northwestern Congo Craton BIFs, associate the lithologies with mainly <250 °C low temperature hydrothermal fluids (Fig. 7C-G). Being a strong component of low temperature shallow-submarine hydrothermal fluids (Breuer and Pichler, 2013), arsenic is also enriched by several orders of magnitude in the Fe-rich carbonates compared to the underlying banded shales with respect to PAAS (Fig. 3P), with normalization to detrital Al suggesting a authigenic or chemical precipitation (Fig. 4I). Authigenic and or chemical enrichment of Eu and Ce is supported by a lack of meaningful correlation between detrital Al, Eu/Eu* and Ce/Ce* anomalies (Fig. S3A-B). With respect to PAAS composition, Eu and Ce are both several times enriched in the Fe-rich carbonates, with similar but muted enrichment in the Mn-rich black shales, sandstones and pyritized black shales relative to the detritus-rich banded shales (Fig. S3C-D). This observation further suggests a more obvious authigenic and or chemical origin for the REEs in the upper metalliferous lithologies, relative to major detrital contribution in the underlying banded shales.

4.3. Paleo-weathering depositional dynamics

An average CIA value of 71.6 % for the studied section (Figs. 4K & 5A), evocative of the 70–75 % UCC shale estimates, indicates overall moderate weathering of source rocks (Fedo et al., 1995; Fedo and Babechuk, 2023), being generally higher for the upper metalliferous

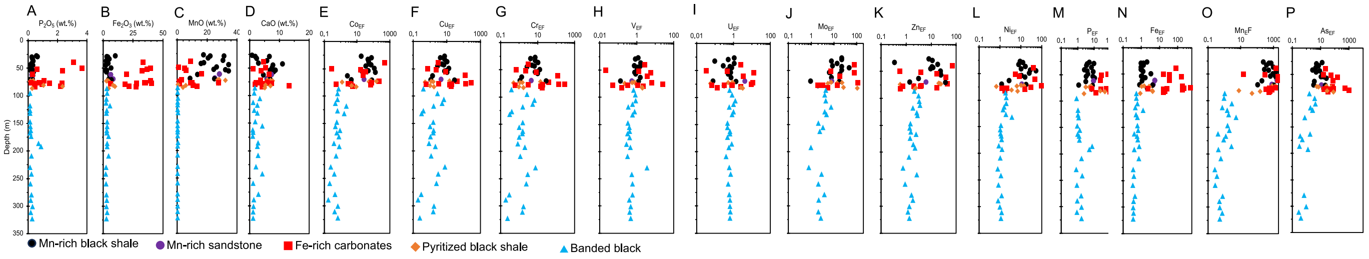

Fig. 3. Major and trace element enrichment patterns up the studied section. Enrichment factors (EF) were calculated according to Tribovillard et al. (2006).

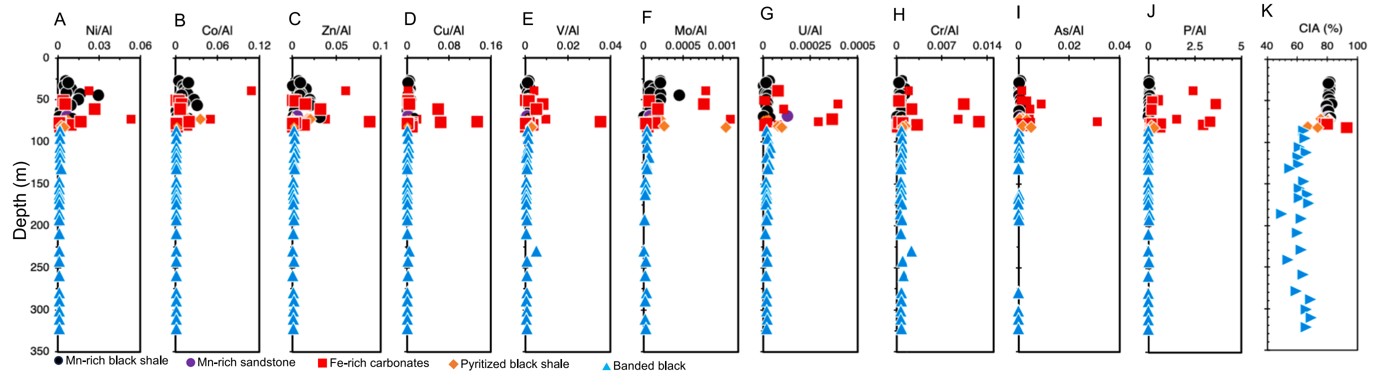

Fig. 4. Authigenic elemental enrichment with respect to the Chemical index of alteration (CIA) weathering and detrital Al proxies. A-J) Trace metal(loid)s and phosphorus concentrations normalized to the Al detrital proxy plotted against depth (sequence/lithostratigraphy) and CIA. K) CIA trends across sequence/lithostratigraphy.

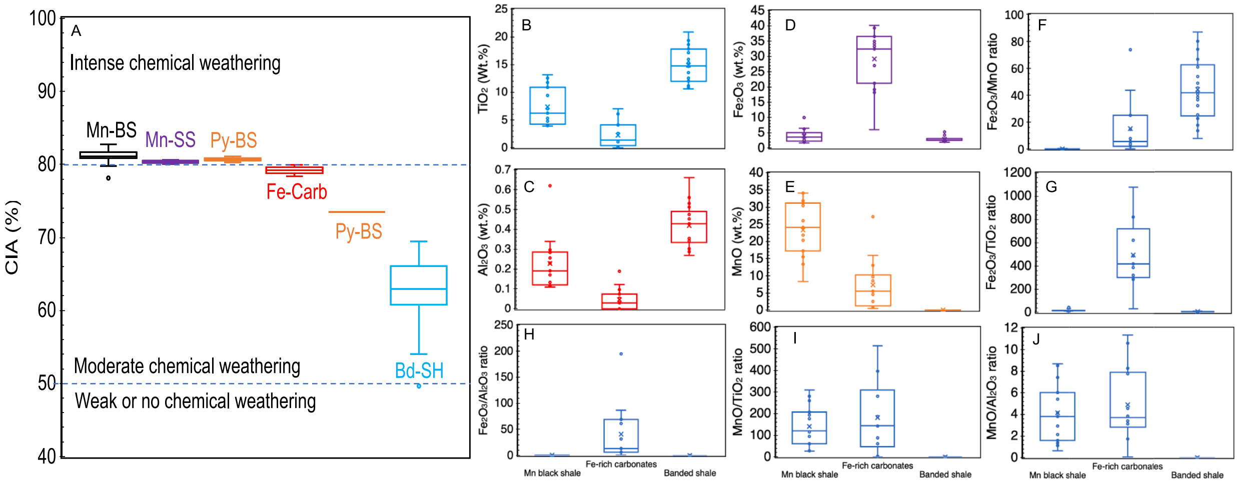

Fig. 5. Bar and whisker diagrams showing the relationship between average CIA and Sequence/lithostratigraphy and total Fe (Fe_2O_3), Mn MnO, TiO_2 and Al_2O_3 in the banded shales, Fe-rich carbonates and Mn-rich black shale units. A) Average distribution of measured CIA weathering indices along sequence/lithostratigraphy, from the underlying banded shales passing upwards through the thin pyritized layer, the Fe-rich carbonates and a second thin pyritized unit, capped by Mn-rich sandstones and black shales. Bars represent standard deviation from the mean. B) Relationship between TiO_2 content and the banded shales, Fe-rich carbonates and Mn-rich black shale units. C) Relationship between Al_2O_3 content and the banded shales, Fe-rich carbonates and Mn-rich black shale units. D) Relationship between Fe_2O_3 content and the banded shales, Fe-rich carbonates and Mn-rich black shale units. E) Relationship between MnO content and the banded shales, Fe-rich carbonates and Mn-rich black shale units. F) Relationship between Fe_2O_3/MnO ratios and the banded shales, Fe-rich carbonates and Mn-rich black shale units. G) Relationship between Fe_2O_3/TiO_2 ratios and the banded shales, Fe-rich carbonates and Mn-rich black shale units. H) Relationship between Fe_2O_3/Al_2O_3 ratios and the banded shales, Fe-rich carbonates and Mn-rich black shale units. I) Relationship between MnO/TiO_2 ratios and the banded shales, Fe-rich carbonates and Mn-rich black shale units. J) Relationship between MnO/Al_2O_3 ratios and the banded shales, Fe-rich carbonates and Mn-rich black shale units. Bd-SH represents banded shales; Py-BS, Pyritized black shales; Fe-Carb, Fe-rich carbonates; Mn-SS, Mn-rich sandstones; Mn-BS, Mn-rich black shales.

facies where CIA averaged 82.5 % for the Mn-rich black shales (Fig. 5A). As already mentioned, TE and ME enrichment correlate well with sequence stratigraphic CIA records. The CIA data tend to plot along the A-CN axis, parallel to expected weathering trends for UCC, TTG and granite, without significant deviation towards the A-K axis, suggesting limited post-depositional K enrichment (Fig. 8A). The samples cluster predominantly in the felsic field, mainly around UCC and TTGs on the compositional discriminant diagrams of Th/Cr versus La/C and Th/Sc versus La/Sc, with associated Al/Ti ratios signifying major contributions from felsic source rocks (Fig. 8B-E). A few samples occupy the limit between mafic and felsic crust, hinting on possible minor involvement of intermediate rock sources. Moreover, Th/Sc versus Zr/Sc and Al_2O_3 versus SiO_2 plots (Fig. S4), together with a mainly felsic crust provenance of the samples (Fig. 8), indicate that the CIA values and the geochemical profiles are not biased by sediment recycling, sorting and lithology above the banded shale boundary. On the other hand, the strong detrital composition of the banded shales is consistent with long-term recycling and sorting. Trace element normalization to the Al detrital proxy associates enhanced chemical weathering of source rocks with the deposition of the upper metalliferous facies (Fig. 4) and increasing dissolution of various trace metals and P in seawater by several orders of magnitude (Fig. 3).

4.4. *Redox depositional conditions*

A combination of C_{org}, $C_{carbonates}$, N, true Ce anomalies, enrichment of redox sensitive TEs and Fe speciation systematics (Figs. 3, 9A-K, S5 & Table S4), delineate two broad redox trends across the studied section. Low and invariant bulk total C_{org} and N systematics evolved from the banded shale to being markedly enriched in the overlying Fe-Mn-rich facies (Fig. 9C, D). This boundary is associated with stable N isotopes switching towards more positive values and C_{org} isotopes towards more negative ratios (Fig. 9B, E). Inferred redox changes and C_{org} isotope distribution correlate well with those of the $FB_{1b\text{-}c}$ unit of the adjacent

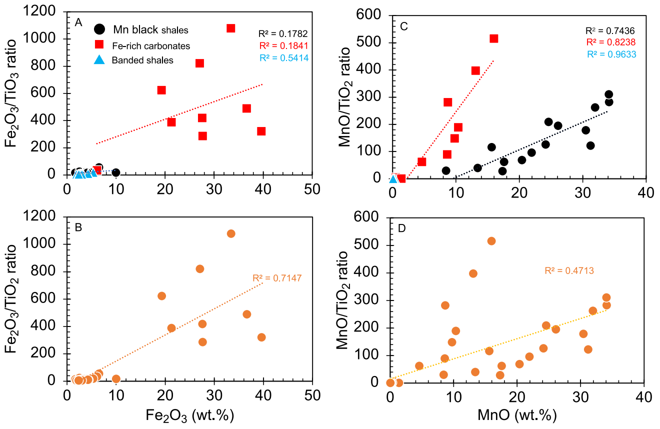

Fig. 6. Cross plots showing the behaviour of Fe_2O_3/TiO_2 and MnO/TiO_2 ratios with respect to Fe_2O_3 and MnO concentrations in the banded shales, Fe-rich carbonates and Mn-rich black shale units. A) Fe_2O_3/TiO_2 ratios showing correlations for the individual banded shales, Fe-rich carbonates and Mn-rich black shale units. B) Fe_2O_3/TiO_2 ratios showing correlations across the banded shales, Fe-rich carbonates and Mn-rich black shale units. C) MnO/TiO_2 ratios showing correlations for the individual banded shales, Fe-rich carbonates and Mn-rich black shale units. D) MnO/TiO_2 ratios showing correlation across the banded shales, Fe-rich carbonates and Mn-rich black shale units.

42 km^2 Bangombe Plateau (Canfield et al., 2013; Ossa Ossa et al., 2018). The banded shales associate with oxic bottom waters and the overlying metalliferous lithologies with seawater redox stratification, characterized by anoxic bottom waters experiencing ferruginous and euxinic conditions (Fig. 9G, H & S5). PAAS normalized REE patterns with negative Ce anomalies are muted in all lithologies, although varying levels of light REE (LREE) depletion and slightly positive La anomalies are discernible (Fig. 7D-G). Association of true Ce anomalies to oxic bottom oxic water deposition of the banded shales (Fig. 9F, K) coincide with oxygenated conditions inferred by Fe speciation analysis (Fig. 9G, H). Enrichment of a multitude of redox sensitive metal(loid)s relative to PAAS is inferred for the upper banded shale transition (Fig. 3H-J), with Mo, U and TOC enrichment suggesting hydrological restriction of the basin (Figs. 3 & 9I, J).

5. Discussion

5.1. *Provenance and facies depositional mechanisms*

5.1.1. *Weathering influence*

According to Fedo and Babechuk (2023), mafic igneous rocks rich in biotite, olivine, pyroxene and amphibole can influence the CIA index. However, provenance analysis suggests a mainly UCC-felsic-TTG affinity for our samples (Fig. 8). With average TTGs containing <5 wt% ferromagnesian elements combined, implies such low ferromagnesian content could not have skewed our observations.

The flattening out of the positive correlation between Zr/Sc and Th/Sc ratios in the banded shales (Fig. S4A) and the <35 Zr/Sc ratios in the upper metalliferous units, together with coeval high CIA values (Fig. 4K & 5A), indicate a primary composition controlled by similar source rock composition and negligible primary sediment reworking (McLennan et al., 1993). This is because polycyclic sediment reworking is often

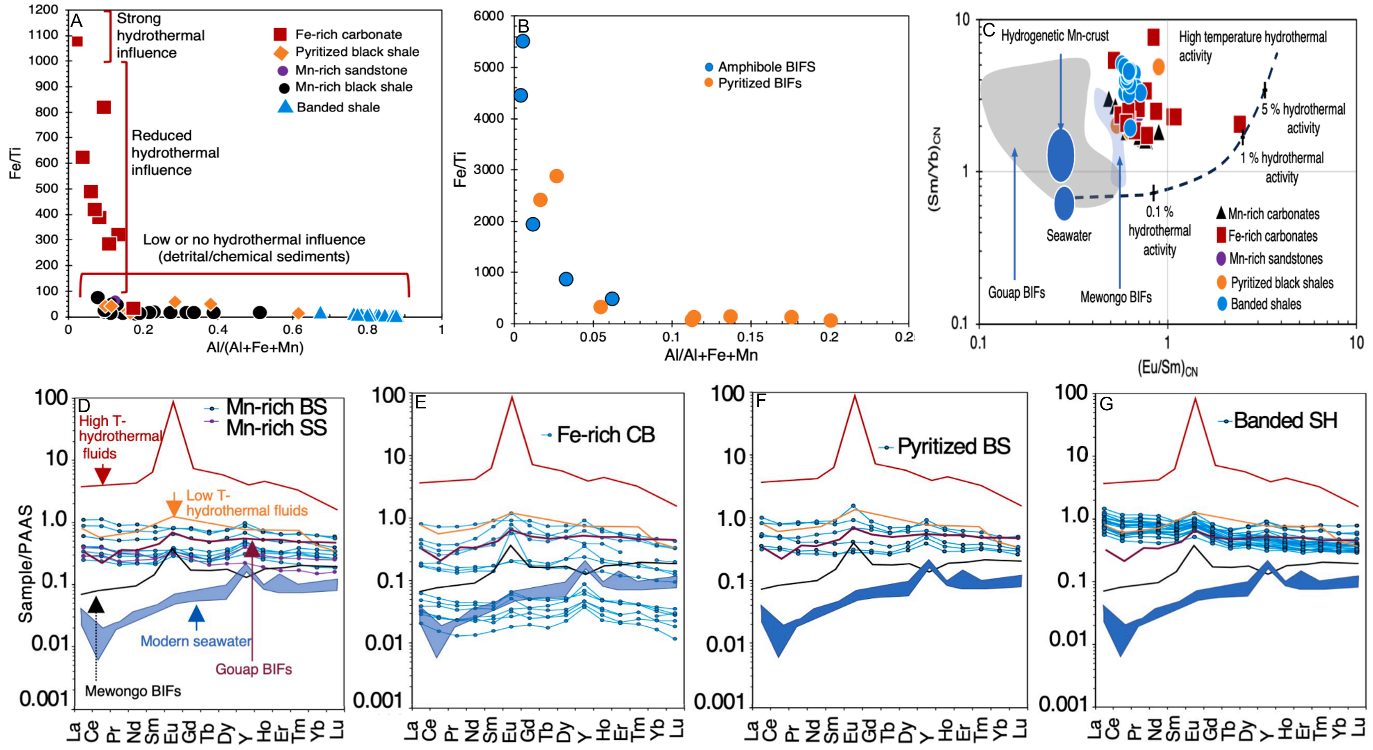

Fig. 7. Link between lithology and hydrothermalism inflence. A) Fe/Ti versus Al/Al + Fe + Mn hydrothermal proxy cross plot. Distinct hydrothermal influence is evident when Fe/Ti is ≥100, combined with low Al/(Al + Fe + Mn) ratios (Boström, 1970; Boström et al., 1972, 1973; Pecoits et al., 2009). B) Fe/Ti versus Al/Al + Fe + Mn plots for the Gouap BIFs of the northwestern margin of the Congo Craton (Soh Tamehe et al., 2021). Ti concentrations of the Mewongo BIFs were below detection limit to allow a similar comparison. C) Chrondrite normalized (CN) Sm/Y versus Eu/Sm cross plots (Alexander et al., 2008; Deassou Sezine et al., 2022). D-G) Rare Earth Element (REE) distribution compared with high and low temperature hydrothermal fluids, modern seawater, and the Paleoproterozoic BIFs of a similar age in the northwest margin of the Congo Craton (Soh Tamehe et al., 2021). Sm/Yb vs Eu/Sm ratios according to Alexander et al., 2008(53). Average hydrothermal fluid REE composition reconstructed according to Bau and Dulski (1999) and compared to modern seawater (Alexander et al., 2008 and references therein). Although the northwest Congo Craton BIFs have experienced metamorphism, their seawater REE and hydrothermal composition has been shown to be preserved (Soh Tamehe et al., 2021, 2022; Deassou Sezine et al., 2022). BS, black shale. SS, sandstone. CB, carbonates. SH, shale.

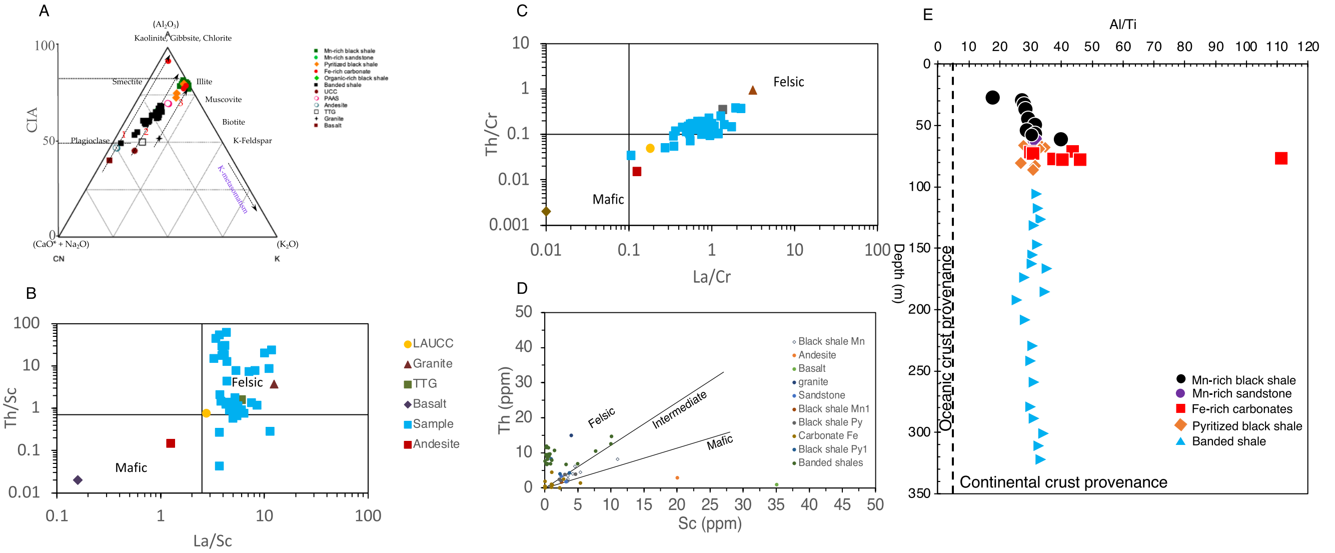

Fig. 8. Paleo-weathering (CIA) and Source provenance reconstruction of the studied facies. A) A–CN–K (Al_2O_3–CaO + Na_2O–K_2O) ternary diagram (Fedo et al., 1995; Fedo and Babechuk, 2023). Arrows 1, 2 and 3 indicate potential weathering trends for basalt and andesite, UCC-TTG and granite, respectively. Data for basalt, andesite, TTG and granite are from Condie (1993). UCC and PAAS data are from Taylor and McLennan (1985). B) Th/Sc versus La/Sc provenance biplots. C) Th/Cr versus La/Cr provenance biplots. D) Th versus Sc provenance biplots. E) Al/Ti ratios plotted against sample depth and stratigraphy, showing that the entire set of samples have a strong terrigenous composition. According to this model, Al/Ti ratios closer to 20 reflect average continental rock values and those nearer 5, weathering products of oceanic rocks (Boström et al., 1969; Boström, 1970).

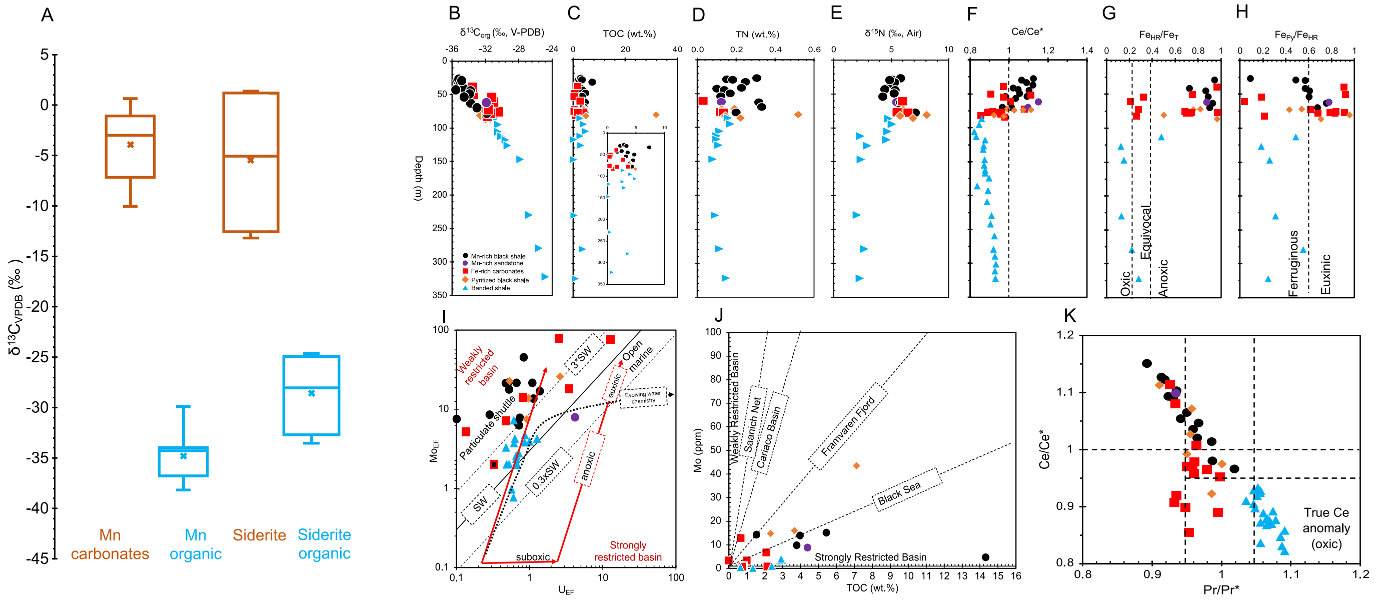

Fig. 9. Redox reconstruction and distribution of organic carbon, bulk nitrogen and their isotopic compositions in the studied cross section. A) Distribution of carbon isotopes in organic carbon and carbonates associated with Fe-Mn-rich carbonate deposits in the FB_1 Formation Member according to Weber and Gauthier-Lafaye (2013). B-C) Organic carbon systematics for the four drill holes analyzed. Inset in panel c shows the spread of the data excluding the pyritized sample with total organic carbon content of up to 31 wt%. D-E) Nitrogen systematics for the four drill holes studied. F) Ce/Ce* versus Pr/Pr* anomalies calculated according to Bau and Dulski (1996). G-H) Iron speciation across sequence stratigraphy. I) Mo versus U enrichment patterns for the four drill core holes studied (Tribovillard et al., 2006; Algeo and Tribovillard, 2009). J) Mo vs TOC cross plot for the drill core holes studied compared to modern marine sediment profiles with different redox and basin restriction properties (Algeo and Lyons, 2006). K) Ce/Ce* versus Pr/Pr* plot for the four drill core holes studied.

accompanied by enrichment of poorly mobile heavy minerals (notably Zr in zircon minerals), while accumulation of stable minerals like quartz dilutes sediment components and elements (McLennan et al., 1993). Immobile Th and Sc on the other hand do not undergo significant fractionation during transport and deposition (McLennan et al., 1993).

According to McLennan et al. (1993), the >35 Zr/Sc ratios in the banded shales are more consistent with primary sediment sorting and recycling, i.e., reworking which enriches quartz (SiO_2) at the expense of clay-size minerals rich in Al_2O_3. The end point of this process can be expressed as rising SiO_2/Al_2O_3 ratios coinciding with falling TE content in facies affected by extensive sediment reworking. Although we see systematic enrichment of SiO_2 and Al_2O_3 progressing from the banded shales to the upper metalliferous sediments (Fig. S4B), the SiO_2/Al_2O_3 ratios suggest SiO_2 is more enriched in the Fe-rich carbonates than Al_2O_3 (Fig. S3C). However, the elevated TE content of the Fe-rich carbonates (Figs. 3-4) does not support primary sediment reworking as the source of

SiO_2 enrichment in this section. Low SiO_2/Al_2O_3 ratios in the Mn-rich lithologies correspond well with elevated TE composition and negligible sediment reworking as corroborated by the Th/Sc versus Zr/Sc cross plots (Fig. S4A). Weak SiO_2/Al_2O_3 ratios in the banded shales (Fig. S4C) due to co-enrichment of SiO_2 and Al_2O_3 (Fig. S4B) are consistent with low TE content (Fig. 3) attributed to primary sediment reworking (Fig. S4A). Overall, succession of low CIA values in the banded shales by stepwise increase up section, suggest the CIA values and geochemical signals of the metalliferous layers reflect increasing chemical weathering more than change in source rocks and primary sediment reworking.

5.1.2. *Hydrothermal influence*

Deposition of the Fe-Mn-rich rocks has been previously attributed to upwelling of deep-sea hydrothermal Fe^{2+}/Mn^{2+}-rich fluids to continental margin waters (Gauthier-Lafaye and Weber, 2003; Ossa Ossa et al., 2018). However, contribution by continental weathering and the source of hydrothermal fluids remain to be co-elucidated. Therefore, we use the Fe/Ti versus Al/(Al + Fe + Mn) ratio to distinguish the primary influence of hydrothermal activity from other sources. This assumption is reliant on the premise that calibration of this proxy against average continental and oceanic crust, active hydrothermal ridge sediments and a mixture of these sources, associates Fe/Ti > 100 and low Al/(Al + Fe + Mn) ratios with hydrothermal fluid influence (Boström, 1970; Boström et al., 1972, 1973; Pecoits et al., 2009). Accordingly, Al/(Al + Fe + Mn) ratios correlate geography with submarine volcanic ridge activity and the distribution of pelagic seawater Al/(Al + Fe + Mn) ratios (Boström et al., 1969; Boström, 1970; Bender et al., 1971).

Our >100 Fe/Ti ratios appear to suggest stronger involvement of hydrothermal activity in the deposition of the Fe-rich carbonates than in the later stage formation of the Mn black shales, with little or no contribution indicated for the banded shales. However, Mn black shale and banded shale Fe/Ti ratios are more diluted by Ti loading compared to the Fe-rich carbonates (Fig. 6A), because of greater contamination by continental detritus. Nevertheless, the Mn black shale Al/(Al + Fe + Mn) ratios are distinctively lower than for the detritus-richer banded shales. The most parsimonious interpretation of these trends is that both the Mn-rich black shales and Fe-rich carbonates experienced more influential hydrothermal activity than the banded shales. However, deposition of the Mn-rich black shales appears to have coincided with gradual waning of hydrothermal activity and increasing detrital supply. This association is supported by initiation of Mn enrichment in sandstones underlining the Mn black shales. Geochemically, the Fe-rich carbonates contain maximum Al/(Al + Fe + Mn) ratios of ~0.2, doubling to >0.5 in the Mn black shales and up to >0.8 in the banded shales. Moreover, connection of the Fe-rich carbonates with greater hydrothermal fluid influence is supported by $(Sm/Yb)_{CN}$ versus $(Eu/Sm)_{CN}$ cross plots in which up to ~1–5 % hydrothermal fluids may have been involved, with a maximum of ~0.1–1 % for the Mn black shales (Fig. 7C).

To further constrain the source and potential hydrothermal fluid temperatures, we consider the estimated depositional age of ~2100–2000 Ma for the FB_{1c} unit, which is believed to coincide with collision of the Congo-São Francisco cratons during the Eburnean-Transamazonian orogeny (Pambo et al., 2006; Barbosa and Sabaté, 2004; Teixeira et al., 2017; dos Santos et al., 2023). Pambo et al (2006) describe a model which juxtaposes the Congo Craton to the Saõ Francisco and the Transamazonian Cratons in Brazil, related to a convergence activity and volcanism, contemporaneous with the onset of orogenesis at ~2100–2040 million years ago. In this model, they propose a broad lack of relief in the Francevillian basin due its location over the subducted crust and therefore out of the orogenic range. Comparisons with modern high and low temperature hydrothermal fluid REE regimes indicate that this tectonic event may have resulted in the deposition of low temperature hydrothermal BIFs on the northwestern Congo Craton margin, Northwest of the Gabonian block to which the Francevillian sub-basin belongs (Soh Tamehe et al., 2021, 2022; Deassou Sezine et al., 2022). The ~2100 Ma Gouap BIFs are thought to represent potential deeper water equivalents of the shallow continental margin Francevillian Mn-rich facies (Soh Deassou Sezine et al., 2022; Soh Tamehe et al., 2022). Our provenance analysis however affiliates the studied section to UCC and TTGs rocks (Fig. 8), although they also display low temperature hydrothermal axial-like fluid Ca enrichment signal and overall relative depletion of K and Mg (Fig. S6).

Compositionally, the northwestern Congo Craton BIFs and the Fe-rich carbonates are moderately depleted in LREEs relative to heavy REEs (HREEs) and express positive Eu anomalies (Fig. 7E). The precipitation of Eu from >250 °C hydrothermal fluids (Bau and Dulski, 1999; Alexander et al., 2008; Soh Tamehe et al., 2021, 2022; Deassou Sezine et al., 2022), imprints positive Eu anomalies when high temperature hydrothermal fluid contribution is ≥0.035 % (Delvigne et al., 2012). However, our broadly mild Eu anomalies are more akin to the generalized records of Proterozoic seawater trends (Planavsky et al., 2010). Further, the true Ce anomalies reflect those of typical Archean-Paleoproterozoic Fe formations (Planavsky et al., 2010). Our true positive Ce anomalies and Fe speciation data are consistent with previous suggestions that the reworked underlying banded shales formed beneath full to partially oxygenated bottom waters, and the succeeding Fe-rich carbonates and the Mn-rich black shales and sandstones beneath predominantly anoxic (ferruginous/euxinic) waters (Canfield et al., 2013; Ossa Ossa et al., 2018).

On the other hand, the northwestern Congo Craton Mewongo BIFs display negative Y anomalies absent in the Gouap BIFs, while positive seawater-like Y anomalies are discernible in the Francevillian facies. The BIFs fall mainly between $(Sm/Yb)_{CN}$ and $(Eu/Sm)_{CN}$ fields indicating dominant seawater influence and ca. <0.1 % hydrothermal fluid contribution (Soh Tamehe et al., 2021, 2022; Deassou Sezine et al., 2022). The Francevillian Fe-Mn-rich facies show a similar dominant seawater signal, with the Fe-rich carbonates being more inclined to greater hydrothermal fluid influence than the Mewongo and Gouap BIFs (Fig. 7C). However, REE compositional analysis suggests that the Gouap BIFs and the Francevillian lithologies may be more identical than the Mewongo BIFs (Fig. 7D-G). Out of the three Paleoproterozoic BIFs described in the northwestern Congo Craton, all containing significantly lower P_2O_5 concentrations compared to the Francevillian Fe-rich carbonates, the Gouap BIFs exhibit the highest bulk P_2O_5 content (Fig. S7). Association of these deposits with low temperature hydrothermal fluids probably reflects seawater mixing with arc-related hydrothermal fluids, following westward subduction of the São Francisco Craton underneath the West Gabonian block during the Eburnean-Transamazonian orogeny (Soh Tamehe et al., 2022).

5.2. *Basin architecture influence*

The CIA values and inferred correlation to upper UCC and TTG source rock composition, combined with exceptional P enrichment in the Fe-rich carbonates (Figs. 3M & 4I), agree with the exposure of 3050–2700 Ma felsic TTG-like granitoids in the northern and southern parts of Gabon, considered to be protoliths of the Francevillian Group facies (Bankole et al., 2020). These rocks share similar Archean ages of 3200–2900 Ma with TTG suites in northwestern Congo and the São Francisco Craton (Barbosa and Sabaté, 2004; Alexander et al., 2008; Deassou Sezine et al., 2022; Teixeira et al., 2017).

Mo, U and TOC enrichment patterns indicate a hydrologically restricted basin architecture for the Francevillian sub-basin (Fig. 9I, J), in agreement with suggestions by Reynaud et al. (2018) and Aubineau et al. (2021), which contrasts with the foreland open ocean facing Nyong Complex of the northwestern Congo Craton. For example, the increasing enrichment of C_{org} at the expense of Mo (Fig. 9J), especially in the anoxic Mn-rich black shales and Mn-rich sandstones, is indicative of strong removal of Mo from a redox stratified water column, without replenishment from deep water sources (Algeo and Lyons, 2006). Molybdenum and C_{org} are well correlated in the underlying oxic banded shales ($R^2 = 0.7490$), followed by no correlation in the overlying Mn-rich Fe carbonates ($R^2 = 0.0052$), before transitioning into a negative linear correlation in the Mn-rich black shales ($R^2 = 0.7002$) (Fig. S8). These trends are consistent with a change from oxic bottom water conditions towards more redox stratified waters reminiscent of an epicontinental sea setting like the Black Sea (Algeo and Lyons, 2006; Algeo and Tribovillard, 2009; Dong et al., 2023a,b). The positive correlation between Mo and C_{org} in the pyritized black shales possibly reflects pyrite's high affinity for Mo in the more intense anoxic conditions that enhanced co-preservation of C_{org}, rather than an increase in seawater Mo concentrations.

Furthermore, the Francevillian sub-basin and the open ocean facing Nyong Complex continental platforms show distinct redox attributes, unique hydrothermal dynamics and different degrees of metamorphic and/or diagenetic influences, suggestive of distinct paleogeographic settings that can explain their divergent elemental enrichment patterns. For example, P_2O_5 content in the Gouap and Mewongo BIFs average 0.18 and 0.06 wt%, respectively (Soh Tamehe et al., 2021; Deassou Sezine et al., 2022), 1.35 wt% for the Francevillian Fe-rich carbonates and 0.3 wt% for the Mn-rich black shales (Table S3). Further, the Fe-rich carbonates contain a lower average Fe content of 33.6 wt% compared to >41 wt% for the Gouap and Mewongo BIFs (Soh Tamehe et al., 2021; Deassou Sezine et al., 2022). Similarly, the Gouap and Mewongo BIFs record average MnO content of 0.15 wt% and 0.03 wt%, respectively, relative to up to 6.1 wt% for the Fe-rich carbonates and 23.7 wt% for the Mn black shales and sandstones. Moreover, the northwestern Congo margin craton BIFs were deposited in relatively oxic deeper waters (Soh Tamehe et al., 2021; Deassou Sezine et al., 2022), while the Fe-Mn-rich Francevillian facies formed in shallow continental margin anoxic waters.

These paleogeographic and tectonic setting influences imply that Francevillian sub-basin and the northwestern Congo Craton were likely connected to different submarine hydrothermal fluid sources and local geological and weathering processes, both controlled by the onset of the Eburnean-Transamazonian orogen.

5.3. Diagenetic influence

Multiple lines of evidence, including negative $\delta^{13}C_{carbonate}$ values in the Mn-rich black shales and siderite in the Fe-rich carbonates, a switch to C_{org} enrichment (Fig. 9A, B) and coupling to more negative $\delta^{13}C_{org}$ (Fig. 9B) and more positive $\delta^{15}N$ values (Fig. 9E) and Ce anomalies (Fig. 9F), anoxia and euxinia (Fig. 9G, H), collectively point to early diagenetic conditions involved in biotic and abiotic alteration of a precursor Fe-Mn oxide reservoir to Fe-Mn carbonates. For example, low negative $\delta^{13}C_{carbonate}$ values of −10 ‰ for the Mn carbonates and −13.4 ‰ for siderite in the Fe-rich carbonates (Fig. 9A), largely suggest a coupling of early diagenetic microbial reduction of Fe-Mn oxides, sulfate and nitrate to the oxidation of C_{org} (Fig. 10B). This is in addition to previously postulated methanotrophic methane oxidation (Weber and

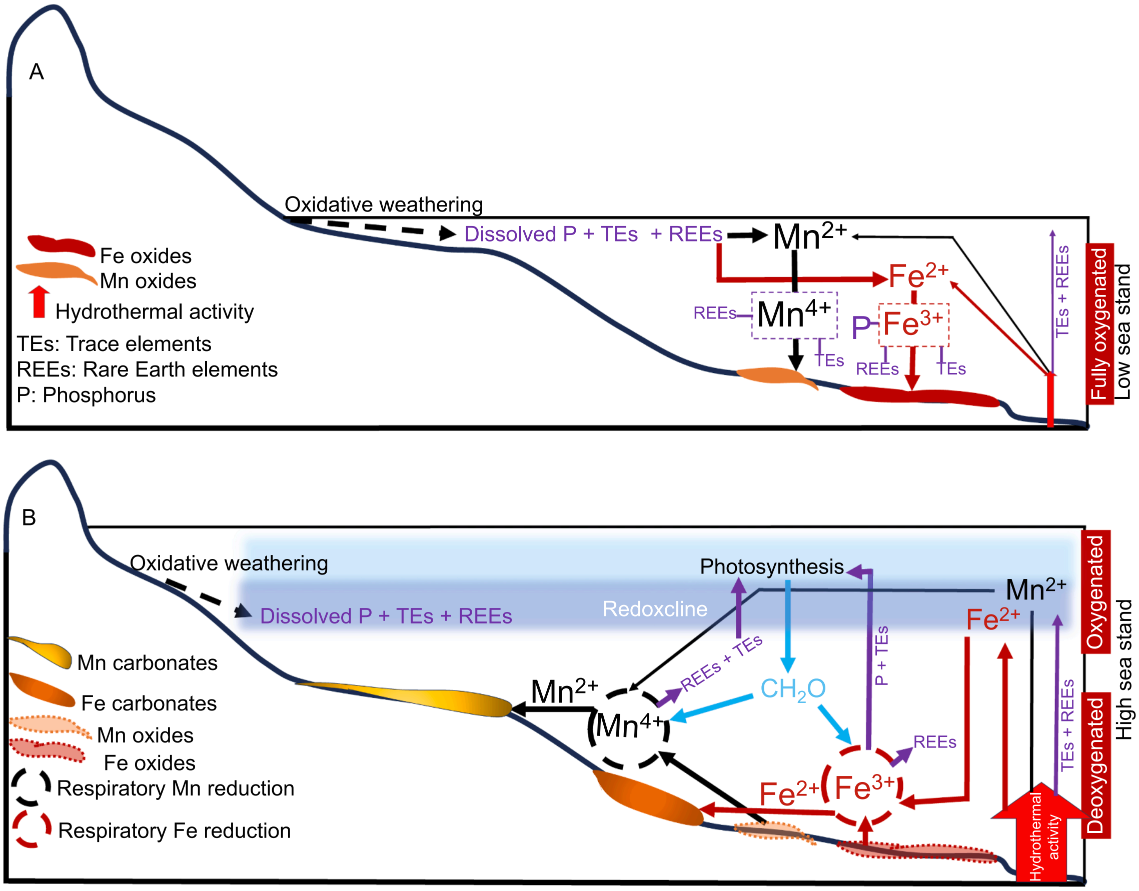

Fig. 10. A conceptual model showing the link between Fe and Mn cycling, redox conditions and hydrothermal activity in the Francevillian sub-basin. A) Fe and Mn cycling in a fully oxic shallow water basin before hydrothermal activity leading to long-term scavenging of P, trace elements (TEs) and rare earth elements (REEs) from seawater by Mn oxides and Fe oxides. B) Water column redox stratification induced by strong hydrothermal activity leading to reductive weathering and recycling of the P-TEs-REEs-rich Fe and Mn oxides, back to seawater. Further dissolution of the Fe-Mn deposits, facilitated by sulfide produced by the sulfate reducing prokaryotes, increased dissolved seawater sulfide concentrations, releasing more TEs and P to seawater. This would have been augmented by continental weathering and TEs supply by hydrothermal emissions. The continued burial of Fe and Mn as carbonates would have reduced the ability of the Fe and Mn oxides to recapture seawater P and bioessential TEs, thereby increasing bioavailability.

Gauthier-Lafaye, 2013). The decomposition of microbial mats in modern settings depletes ^{13}C in carbonates (Sanz-Montero et al., 2023). Moreover, the Mn carbonate and siderite $\delta^{13}C_{carbonate}$ fall within the range of diagenetic biogenic methane production and C_{org} oxidation in modern ferruginous environments (Vuillemin et al., 2023).

Reduction of Fe oxides by the dissimilatory Fe-reducing bacteria with C_{org} under anoxic conditions produces biogenic δ^{13}C-depleted siderite ($FeCO_3$) with isotopic values of <-10 ‰ (Zhang et al., 2001). Low $FeCO_3$ δ^{13}C values could also originate from dissolved inorganic C (DIC) in hydrothermal-seawater-mantle fluid mixtures with a δ^{13}C of ca. −6.5 ‰ or from kinetic isotope fractionation when $FeCO_3$ precipitates directly from seawater-derived DIC (Jiang et al., 2022). For instance, the observed shift to positive Ce/Ce* anomalies in the Fe-Mn-rich lithologies, is a diagenetic $MnCO_3$ and $FeCO_3$ enrichment signature (Huang et al., 2022; Jiang et al., 2022; Dong et al., 2023a,b; Mhlanga et al., 2023). Typically, Ce prevails as tetravalent ions in oxygenated seawater, being less soluble and more reactive with Mn and Fe oxides than other REEs (Bau and Dulski, 1999). The ensuing <1 Ce/Ce* in oxygenated seawater is reflected in the oxic banded shales, being >1 in the anoxic metalliferous facies. In this scenario, highly reactive Fe (Fe_{HR}) to total Fe (Fe_T) and pyrite Fe (Fe_{py}) to Fe_{HR} ratios mirror comparable bottom water anoxia for the correlative Bangombe Plateau (Canfield et al., 2013).

A similar diagenetic model involving the reduction of a seafloor ferromanganese oxides linked to changing redox conditions, was recently proposed for dolostones associated with Fe-Mn enrichment in the correlative FB Formation in the Lastoursville sub-basin (Yoshida et al., 2023). This observation suggests a basin-wide mechanism for the deposition of Fe and Mn in the Francevillian group. Differences in mineralogical enrichment patterns between the Lastoursvillian and Francevillian sub-basins are probably related to a complicated basin architecture that resulted in the deposition of the Francevillian Group in four distinct rift basins probably characterized by horsts and grabens, in Franceville, Okondja, Lastoursville and Booué (Weber, 1968; Feybesse et al., 1998; Pambo et al., 2006; Yoshida et al., 2023).

In this diagenetic model, formation of the precursor Fe-Mn oxides (Fig. 10A) was probably aligned with the widespread oxic conditions that preceded deposition of the Fe-rich carbonates (Yoshida et al., 2023). Moreover, the observed primary sediment reworking that marks the banded shales implies progressive loss of soluble elements into solution could have contributed to systematic enrichment in seawater and subsequent incorporation and precipitation into precursor seafloor Fe-Mn oxides. The Fe-Mn oxides were then later transformed to Fe-Mn carbonates when anoxic hydrothermal fluids overwhelmed bottom waters and sea level rise (Canfield et al., 2013; Ossa Ossa et al., 2018; Reynaud et al., 2018; Yoshida et al., 2023) promoted shoaling of anoxic conditions (Fig. 10B). In addition to this already existing seafloor Fe-Mn deposit, the onset of hydrothermal activity likely supplied additional hydrothermal Fe and Mn that was oxidized in the redoxcline to form surplus Fe-Mn oxides that was further transformed into Fe-Mn carbonates beneath the redoxcline and in the unconsolidated sediment pile during early diagenesis (Fig. 10B). It is well-established that Fe-Mn oxide reductive processes in unconsolidated sediments enrich P, Mn^{2+} and Fe^{2+} in overlying anoxic bottom waters.

The seafloor altered Fe-Mn sources were likely separated both temporally and spatially, considering that under anoxic conditions, faster reductive dissolution of Mn over Fe oxides should first result in preferential deposition of the Mn-rich black shales and sandstones before the Fe-rich carbonates, which is not observed. It is also possible that formation of some of the Fe-Mn carbonates could have bypassed the Fe-Mn oxide phase if alkalinity produced by microbial oxidation of C_{org} beneath the redoxcline was sufficient to allow this to happen (Roy, 1992; Wittkop et al., 2020).

Our data suggest that chemical weathering of an inferred felsic protolith proximal to or in shallow submerged oxygenated platforms, probably allowed oxidative weathering to progressively enrich the seafloor with Fe-Mn oxides and co-drawdown of P and bioessential TEs and REEs from seawater (Fig. 10A; Klinkhammer et al., 1983; Calvert and Pedersen, 1996; Wheat et al., 1996, 2003; Feely et al., 1998; Kuhn et al., 1998; Yoshida et al., 2023). Under these oxic conditions, V, U and Mo would have been released by oxidative weathering into seawater (Tribovillard et al., 2006). In conditions accompanied by strong oxidation of reduced Fe and Mn and high C_{org} content, Mo, V and U are co-enriched in Fe-Mn oxide/C_{org}-rich sediments (e.g., Anderson, 1982; Hein et al., 1997). Increasing enrichment of Mo over U is expected in bottom water euxinic sediments (Fig. S5; Algeo and Maynard, 2004; Tribovillard et al., 2006).

Further, the high affinity of Ce(IV) formed in oxic waters to bind Fe-Mn oxides, C_{org} and clays, would have resulted in shuttling to bottom waters and eventual burial in seafloor sediments (Byrne and Sholkovitz, 1996; Kuhn et al., 1998). This interpretation is supported by co-enrichment of $C_{org,}$ REEs and various redox sensitive trace metals in the metalliferous horizon. It is thought that remobilization from similar sources concentrated REEs in Paleoproterozoic redox stratified bottom waters (Planavsky et al., 2010). Like U, V and Mo enrichment, positive Ce anomalies characterize the upper banded shale boundary that marks a sharp transitional boundary from oxic to redox stratified water mass. Moreover, the recognized absence of positive Ce anomalies in hydrothermal fluids (Klinkhammer et al., 1983; Kuhn et al., 1998) supports the shuttling of Ce by potential Fe-Mn oxides to the seafloor, followed by later diagenetic enrichment in the Fe-Mn carbonates.

The possibility also exists that the Mn-rich black shales formed through partial ventilation and alteration of an unidentified sulfidic sediment source according to the model of Dong et al. (2023a,b). However, large scale Mn carbonate deposits are predominantly formed in anoxic sediments below oxygenated surface waters in nearshore continental margin environments, where they are enriched via a surface Mn oxyhydroxide shuttle (Calvert and Pedersen, 1996). Moreover, sequential deposition of the Fe-rich carbonates in combination with greater seawater nutrient enrichment is more agreeable with immediate deposition of C_{org}-rich pyritized black shales above the Fe-rich carbonates. As explanation, the ensuing enrichment of seawater with P and trace metal nutrients would have stimulated intense primary production in surface waters (Fig. 10B). Reduced hydrothermal fluid intrusion, together with high surface water C_{org} production would have intensified further deoxygenation of deeper waters by coupling microbial consumption of oxygen to the oxidation of C_{org}, in turn enabling microbial pyrite deposition. According to this model, precipitation of the Mn-rich facies would only have become permissible when these extreme reducing conditions abated to enable deposition.

5.4. *Nutrient enrichment influence*

Phosphorus could have been supplied by hydrothermal plumes following alteration of seafloor basalts by anoxic hydrothermal fluids (Syverson et al., 2021; Rasmussen et al., 2021), in addition to major riverine delivery to surface waters (Sharoni and Halevy, 2022). However, the probability of enriching up to ~4 wt% P in the Fe-rich carbonates by alteration of seafloor basaltic rocks by anoxic hydrothermal fluids alone—i.e., bypassing the Fe oxide enrichment phase—is not supported by our provenance analysis. Moreover, it is suggested that seafloor weathering on its own contributes only a small fraction of P to seawater with the chemical weathering of continental silicates being the dominant input (Wheat et al., 1996, 2003, 2008; Sharoni and Halevy, 2022). The latter observation aligns with lack of evidence pointing to major P supply to paleo-marine waters by seafloor weathering to a level comparable with the Francevillian records (Fig. 11; Reinhard et al., 2017). Otherwise, this mechanism which would have been more prevalent in anoxic Archean-Paleoproterozoic seawater subjected to greater hydrothermal fluid influence, should have recorded similarly high P levels in marine sedimentary records spanning the Precambrian oceans (Planavsky et al., 2010).

Moreover, the greater chemical weathering indices recorded in the

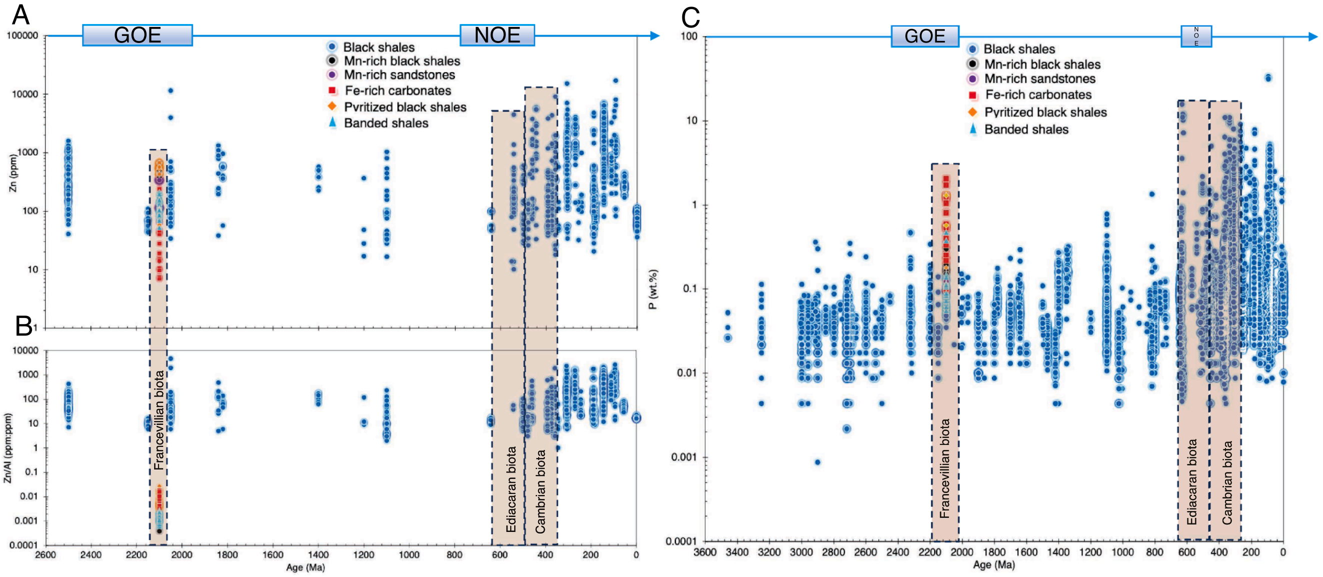

Fig. 11. Log normal comparison of Zn and P composition for samples with published marine shale values through Earth history. A) Zn concentration in ppm. B) Zn concentration normalized to Al as a detrital and authigenic enrichment proxy. C) Sample P data plotted in weight percent P concentrations compared to marine shales through Earth history. The Zn and P data are adapted from Scott et al. (2013) and Reinhard et al. (2017), respectively.

Mn black shales and Fe-rich carbonates are not coeval with comparable P_2O_5 enrichment despite their similar rock source provenance. Therefore, a change in source rock composition cannot explain the distinct coupled Fe, Mn and P enrichment patterns. Likewise, a mainly detrital origin for apatite concentrated in the Fe-rich carbonates (Mossmann et al., 2005) cannot be justified since the Mn black shales and sandstones show a greater detrital influence than the Fe-rich carbonates. Moreover, apatite enrichment in the Mn-rich black shales should be greater if the more negative $\delta^{13}C_{org}$ values in the Mn black shales and sandstones are indicative of greater microbial remineralization of P-rich organic matter. However, this is not the case. When viewed in this light, enrichment of up to 4 wt% P in the Fe carbonates suggest unique feedback mechanisms existing between the P and Fe biogeochemistry, decoupled from Mn cycling. The absence of correlation between P and TOC concentration (Fig. S9A) is consistent with low C/P ratios in the Fe-rich carbonates (Fig. S8B), likely reflects lower sedimentation rates and oxidation of C_{org} (Ingall and Van Cappellen, 1990).

The most parsimonious mechanism for P enrichment in the Fe-rich carbonates therefore points to diagenetic alteration of a distinct seafloor P-rich Fe oxide reservoir by dissimilatory iron reducing microbes and sulfide produced by sulfate reducers in bottom water reducing conditions. In this model, systematic burial of Fe carbonates and pyrite retained P in solution at the expense of Fe oxide dissolution (Fig. 10B). The resulting saturation of dissolved P at the seawater-sediment interface would have triggered apatite precipitation (Ruttenberg and Berner, 1993; Ruttenberg, 2003).

Our bulk Zn, Cu and Mo concentrations are consistent with historical paleo-dynamic marine black shale archives (Figs. 11A & S10-S11). However, much lower Zn/Al ratios across the sampled section suggest that seawater dissolved Zn concentrations may have been much inferior in the Francevillian sub-basin compared to similar contemporaneous settings and that the upper banded shale boundary coincided with a rise in dissolved seawater Zn content (Fig. 11B). Despite this overall lower dissolved seawater Zn content, quantitative Zn enrichment and fractionation of light Zn isotopes is recorded in macrofossils located in the strata immediately above the studied facies (El Albani et al., 2023; Ossa Ossa et al., 2023). This observation appears to fall in line with the hypothesis that the evolution of biological Zn usage was perhaps controlled by cellular requirement than dynamic changes in seawater levels (Robbins et al., 2013). For instance, Zn biolimitation in some cyanobacteria is managed by replacing Zn with Co (Saito et al., 2003), which tends to be more enriched relative to Zn at the upper banded shale boundary (Fig. S12). Similarly, some unicellular eukaryotes adapt to Zn deficiency by upregulating the expression of high-affinity Zn uptake systems and substituting Zn for Co and Cd (Timmermans et al., 2001; Kellogg et al., 2020, 2022).

Bulk P enrichment in our samples is comparable to coeval records in this interval (Fig. 11C). The data highlight potential seawater P concentrations equivalent to or nearing Ediacaran marine biosphere levels and beyond, a time when undisputed metazoans first appeared in the marine sedimentary rock record (Reinhard et al., 2017; Laakso et al., 2020; Dodd et al., 2023). Considering the biogenic bridge between environmental change, seawater P content, trophic level complexity and body size with oxygenation (Laakso et al., 2020; Wang et al., 2020; Dodd et al., 2023), it is quite likely that localized environmental change in Franceville, together with a rise in dissolved seawater P content and oxygenation, might explain the subsequent explosion of aerobic macroscopic life in the overlying FB_2 formation in the Francevillian sub-basin.

The associated P/Al ratios point to maximum authigenic P enrichment during deposition of the Fe-rich carbonates, intermediate in the Mn-rich carbonates, sandstones and pyritized shales, and lowest in the banded shale interval (Fig. S13). The latter probably reflects contribution by sediment reworking (Fig. S4A). Our fine-grained shales record sediment geochemistry in a near continental margin marine environment, associated with significant authigenic P enrichment together with various bioessential metals in shallow marine waters. This contrasts with the relatively insignificant authigenic P enrichment reported by Reinhard et al. (2017) in shales of a similar age sampled from elsewhere (Fig. 11C), pointing to a unique local nutrient enrichment event in the Paleoproterozoic Francevillian sub-basin. The lower P content of the Mn-rich facies (Fig. 3M) further indicates that these seawater eutrophic conditions began to equilibrate up sequence to enable bottom water ventilation. The appearance of full oxic bottom waters in the immediate overlying FB_2 Member (Canfield et al., 2013; Ossa Ossa et al., 2018), together with macrofossils (El Albani et al., 2010, 2014, 2019), and the proliferation of benthic microbial mats (Aubineau et al., 2018, 2019, 2021), represent a potential hallmark of this transitionary boundary.

5.5. Nitrogen cycling influence

Nitrogen and carbon systematic (Figs. S14-S15), showing a moderate linear covariation ($R^2 = 0.35$) between increasingly negative $\delta^{13}C_{org}$ and positive $\delta^{15}N$ enrichment (Fig. 9B, E & S14B), appear to suggest a weak but enhanced coupling between heterotrophic assimilation and reduction of ^{14}N-^{12}C-rich C_{org}. This is because non-quantitative reduction of fixed ^{14}N and elimination as N_2 from bottom anoxic waters and sediments, enrich sediments with ^{15}N as a by-product.

As a whole, oceanic planktonic biomass has an average molar C/N ratio of ~7 (Redfield, 1958), with biomass remineralization in the water column and sediments producing higher sedimentary molar C/N ratios. The predominantly 2 to 91 M C/N ratios in our samples (Table S6; Fig. S15) are consistent with those of other Francevillian facies (Aubineau et al., 2021; Kipp et al., 2018; Ossa Ossa et al., 2022), and hint at diagenetic reworking of primary biomass. In addition, remineralization of N-rich organic matter may release ammonium (NH_4^+) to pore waters that can be subsequently incorporated into phyllosilicates via substitution for K cations, with further fractionation of $\partial^{15}N$ (Williams et al., 1995). Nonetheless, the lack of apparent correlation between TN and K (Fig. S14A), suggests negligible influence for phyllosilicate-bound N phases on the $\partial^{15}N_{bulk}$ values.

The C and N isotope composition in sedimentary rocks is also sensitive to thermal alteration induced by diagenesis and metamorphism (Ader et al., 2006). However, the Francevillian sub-basin is well-known for little or no metamorphic overprinting. During thermal diagenesis, breakdown and volatilization of organic molecules enriches the residual pool with heavy C and N isotopes (Bebout and Fogel, 1992; Stüeken et al., 2017). This enrichment causes a shift in $\partial^{15}N_{bulk}$ values by <1 ‰ in lower greenschist facies that are not present in our samples. Moreover, increasing $\partial^{15}N_{bulk}$ value should coincide with decreasing $\partial^{13}C_{org}$, and it is expected that thermal alteration should promote N depletion relative to C as well as coeval decrease in TOC and ^{12}C. These conditions are typically represented by strong covariation between $\partial^{13}C_{org}$ and TOC, $\partial^{13}C_{org}$ and C/N, $\partial^{15}N_{bulk}$ and TN, $\partial^{15}N_{bulk}$ and C/N, as well as $\partial^{13}C_{org}$ and $\partial^{15}N_{bulk}$, none of which is observed across sampled section (Fig. S14B-F). The identification of randomly ordered diagenetic illite/smectite mixed-layer clays (i.e., persistence of smectite) in <2 μm clay-size fraction in the Mn black shales, have been interpreted as evidence for lack of significant post-depositional thermal alteration (Ngombi Pemba et al., 2014; Ikouanga et al., 2023).

Modern oceans are dominated by aerobic N cycling in which nitrate is the dominant dissolved species (Stüeken et al., 2016). Nitrification followed by non-quantitative denitrification and/or anammox (anaerobic ammonium oxidation coupled to nitrite reduction) in oxygen minimum zones are microbial N pathways invoked to explain modern positive $\partial^{15}N$ values (Dalsgaard et al., 2005; Sigman et al., 2009). On the other hand, biological N_2 fixation preserves $\partial^{15}N_{bulk}$ values of −2.0 and +1.0 ‰ (Bauersachs et al., 2009; Zhang et al., 2014). High seawater ammonium (NH_4^+) concentration in anoxic waters, together with intense uptake of NH_4^+ into biomass, can tune down biomass $\delta^{15}N$ towards more negative values (Wang et al., 2023). Nonetheless, it is well established that increasing positive $\delta^{15}N$ values correlate broadly with a large nitrate pool coupled to active but non-quantitative denitrification and anoxia (Wang et al., 2023). The switch to more positive $\delta^{15}N$ coinciding with greater N enrichment in the metalliferous facies therefore suggests presence of a sizeable seawater nitrate reservoir due to enhancement of N fixation in surface waters. In this context, a rise in surface water primary productivity, oxygenation and bottom water anoxia should be consistent with the shift towards sedimentary enrichment of N and more positive $\delta^{15}N$ (Fig. 9D, E). This observation agrees well with the two-step dynamic redox change documented by Fe, Ce and redox sensitive trace metal trends.

Considering invariable atmospheric N isotope composition over the last ~3.0 billion years (Marty et al., 2013; Sano and Pillinger, 1990), positive $\partial^{15}N_{bulk}$ values in the range of +2.0 and +5.0 ‰ (average +3.2 ± 1.2 ‰, n = 10) in the Francevillian FB_{1b} unit banded shales could reflect the preservation of an aerobic N cycle coupled to reductive N cycling. The Fe_{HR}/Fe_T ratios <0.22, together with low enrichment levels of redox-sensitive Mo, V, and U in the FB_{1b} banded shales, support deposition under oxygenated bottom waters. Nonetheless, the $\partial^{15}N_{bulk}$ values of the FB_{1b} unit are lower compared to those varying between +4 and +8 ‰ in the Francevillian FC Formation, linked to pervasive and stable aerobic N cycling (Kipp et al., 2018; Ossa Ossa et al., 2022).

Bioavailable Fe, P, and N are primary biolimiting nutrients that control biological productivity over time (Capone and Hutchins, 2013; Reinhard et al., 2017; Tyrrell, 1999). We observe a moderate P enrichment (mean EF_P = 1.7, n = 20) in the banded shales, while Fe is moderately depleted (mean EF_{Fe} = 0.5, n = 23) with respect to PAAS. This indicates that Fe limitation in the FB_{1b} offshore environments could have hampered rates of marine productivity to some degree. Typically, N fixation by the nitrogenase enzyme is dependent on V, Fe and Mo (Hernandez et al., 2008; Zhang et al., 2014; Darnajoux et al., 2019). Our data show that these metals were enriched in seawater upon transition from the banded shales into the Fe-rich carbonates (Fig. 3B, H, J). Combined with the fundamental role of Mn in the splitting of water during oxygenic photosynthesis (Fischer et al., 2015) and the critical role of P in primary production (Tyrrell, 1999), the nutrient-rich conditions at the upper banded shale boundary would have intensified primary production in surface waters, intense N fixation, abundant C_{org} production and surface water oxygenation. These eutrophic conditions would have promoted the enrichment of positive but low $\partial^{15}N_{bulk}$ values (<5‰) in the FB_{1b} unit. This is because preferential nitrogen fixation by the Mo dependent nitrogenase enzymes does not strongly fractionate N, while strong denitrification of nitrate and anammox imparts a positive $\partial^{15}N$ to residual sediment N content (Stüeken, 2013; Wang et al., 2023).

The overlying FB_{1c} lithologies, marked by higher $\partial^{15}N_{bulk}$ values (average +5.7 ± 0.9 ‰, n = 21), together with ferruginous and sulfidic anoxic bottom water conditions resulting from upwelling of trace metal-P-rich fluids (Figs. 3-5), reflect an intensification of deoxygenation of the water column through partial loss of nitrate during denitrification at the redoxcline. The tremendous discharge of nutrients and anoxic waters would have likely shifted the redoxcline upwards. This basin-scale deoxygenation in the FB_{1c} unit would have subsequently led to the observed short-lived nitrate scarcity in the overlying FB_2 Member, as hypothesized by Aubineau et al. (2019) and confirmed by Ossa Ossa et al. (2022).

5.6. Carbon cycling influence

Understanding the geodynamic evolution of the Francevillian group has considerable implications for unravelling processes that drove permanent oxygenation of the atmosphere during the GOE (Poulton et al., 2021). This is because the Francevillian group is a rare paleogeographic setting enclosing the Lomagundi Event (LE)—a time when oxygen is thought to have first risen permanently in the atmosphere (Kump et al., 2011; Canfield et al., 2013; Ossa Ossa et al., 2018; Mayika et al., 2020; Poulton et al., 2021). Unresolved debates suggest the extreme negative $\delta^{13}C_{org}$ values of <−40 ‰ in the Francevillian sub-basin may reflect oxidative weathering of an ancient uplifted C_{org} reservoir deposited in the early stages of the LE (Kump et al., 2011; Canfield et al., 2013). However, no evidence exists to support an uplift event, while Weber and Gauthier-Lafaye (2013) invoke methanotrophic activity.

Our data suggest that negative $\delta^{13}C_{org}$ excursion in the Francevillian Group was initiated somewhere at the top of the banded shales succession, before intensifying up section in conjunction with hydrothermal activity and authigenic P enrichment. Considerable C_{org} production in surface waters is mirrored by increasing C_{org} burial in the upper metalliferous lithologies and negative $\delta^{13}C_{org}$ covariation (Fig. 9B, C). Similar observations for the oxidation of seawater derived C_{org} in the Lastoursville sub-basin (Yoshida et al., 2023), further argues against the uplift-oxidative weathering of an ancient C_{org} model (Kump et al., 2011). Instead, our data suggest that the upwelling of abundant dissolved nutrient fluids stimulated primary productivity in the continental margin surface waters. The released C_{org} invigorated anaerobic microbial activity, with biological methane cycling and anaerobic C_{org} oxidation contributing to negative $\delta^{13}C_{org}$ enrichment in the sediments, sulfate reduction to pyrite formation, dissimilatory Fe and Mn oxide reduction to Fe-Mn carbonate deposition, and fixed N reduction to positive $\delta^{15}N$ enrichment.

6. Conclusions

The results of this study indicate that the Paleoproterozoic Francevillian sub-basin was hydrologically restricted and even cut off from the global ocean to sustain stable nutrient enrichment and exchange over extended periods. In these conditions, up section dissolved P enrichment and the proliferation of benthic microbial mat feeding grounds would have provided a natural nutrient-rich laboratory for biological experimentation with allopatric speciation to achieve more complex macrobiological proportions. This evolutionary experiment is suggested to have been triggered by a combination of tectonic processes that drove nutrient enrichment and recycling, culminating in local seawater enrichment with P. These observations make it possible that the appearance of macrofossils in Franceville may mark a unique window into our understanding of conditions that enabled and restricted the evolution and disappearance of Earth's earliest macrobiological life forms. Particularly, the broadly anoxic and nutrient-poor Paleoproterozoic Ocean water mass, together with potential confinement of the Francevillian sub-basin, would have presented difficult conditions for the Francevillian biota to take a permanent and global foothold (e.g., Reinhard et al., 2016). When coupled to the absence of similar manifestations in the mostly anoxic nutrient-deficient interval bracketing the Francevillian and Ediacaran biotas, our observations imply that complex macrobiological forms may have evolved at least twice in Earth history—i.e., shortly after the GOE and the NOE. These conclusions draw support from recent Zn systematics (El Albani et al., 2023; Ossa Ossa et al., 2023) and genomic dating (Craig et al., 2023) swinging the needle for when eukaryotic life potentially first emerged from ~1700 Ma towards ~2100 Ma.

CRediT authorship contribution statement

Ernest Chi Fru: Writing – review & editing, Writing – original draft, Visualization, Validation, Supervision, Resources, Methodology, Funding acquisition, Formal analysis, Data curation, Conceptualization. **Jérémie Aubineau:** Writing – review & editing, Investigation, Formal analysis. **Olabode Bankole:** Writing – review & editing, Investigation, Formal analysis, Data curation. **Mohamed Ghnahalla:** Writing – review & editing, Formal analysis. **Landry Soh Tamehe:** Writing – review & editing, Formal analysis. **Abderrazak El Albani:** Writing – review & editing, Validation, Supervision, Resources, Project administration, Methodology, Investigation, Funding acquisition, Formal analysis, Data curation, Conceptualization.

Declaration of competing interest

The authors declare that they have no known competing financial interests or personal relationships that could have appeared to influence the work reported in this paper.

Data availability

Data will be made available on request.

Acknowledgements

We thank the Region Nouvelle Aquitaine, the Centre National pour la Recherche Scientifique and Technique du Gabon (CENAREST), the General Direction of Mines and Geology of Gabon, the Agence Nationale des Parcs Nationaux du Gabon, the University of Masuku, the COMILOG and SOCOBA Companies, the French Embassy at Libreville, and the Institut Français du Gabon, for their support. l'Agence Nationale de la Recherche Scientifique (ANR-BIOGEN) and the French government program (Investissements d'Avenir EUR INTREE, ANR-18-EURE-0010) for their support. The European Research Council (ERC) Seventh Framework (F7) program is acknowledged under grant number 336092. We thank, Oslisly, R., Ngomonda, A., Lebailly, C., Trentesaux, A. and Pambo, F., for support, and Fontaine, C., Laforest, C., Ramaroson, G., Tromas L. and Ventalon, S., for technical assistance.

Appendix A. Supplementary data

Supplementary data to this article can be found online at https://doi.org/10.1016/j.precamres.2024.107453.

References

Ader, M., Cartigny, P., Boudou, J.-P., Oh, J.-H., Petit, E., Javoy, M., 2006. Nitrogen isotopic evolution of carbonaceous matter during metamorphism: Methodology and preliminary results. Chem. Geol. 232, 152–169.

Alcott, L., Mills, B.J.W., Bekker, A., Poulton, S.W., 2022. The great oxidation event facilitated by the rise of sedimentary phosphorus recycling. Nat. Geosci. 15, 2010–2215.

Alexander, B.W., Bau, M., Andersson, P., Dulski, P., 2008. Continentally derived solutes in shallow Archean seawater: rare earth element and Nd isotope evidence in iron formation from the 2.9 Ga Pongola Supergroup South Africa. Geochim. Cosmochim. Acta 72, 378–394.

Algeo, T.J., Lyons, T.W., 2006. Mo-total organic carbon covariation in modern anoxic marine environments: Implications for analysis of paleoredox and paleohydrographic conditions. Paleoceanography 21, PA1016.

Algeo, T.J., Maynard, J.B., 2004. Trace-element behavior and redox facies in core shales of Upper Pennsylvanian Kansas-type cyclothems. Chem. Geol. 206, 289–318.

Algeo, T.J., Tribovillard, N., 2009. Environmental analysis of paleoceanographic systems based on molybdenum–uranium covariation. Chem. Geol. 268, 211–225.

Anderson, R.F., 1982. Concentration, vertical flux, and remineralization of particulate uranium in seawater. Ceochim. Cosmochim. Acta 46, 293–1299.

Anderson, R.P., Tarhan, L.G., Cummings, K.E., Planavsky, N.J., Bjørnerud, M., 2016. Macroscopic structures in the 1.1 Ga continental copper harbor formation: concretions or fossils? PALAIOS 31, 327–338.

Aubineau, J., El Albani, A., Chi Fru, E., Gingras, M., Batonneau, Y., Buatois, L.A., Geffroy, C., Labanowski, J., Laforest, C., Lemée, L., Mángano, M.G., Meunier, A., Pierson-Wickmann, A.-C., Recourt, P., Riboulleau, A., Trentesaux, A., Konhauser, K. O., 2018. Unusual microbial mat-related structural diversity 2.1 billion years ago and implications for the Francevillian biota. Geobiology 16, 476–497.

Aubineau, J., El Albani, A., Bekker, A., Somogyi, A., Bankole, O.M., Macchiarelli, R., Meunier, A., Riboulleau, A., Reynaud, J.-Y., Konhauser, K.O., 2019. Microbially induced potassium enrichment in Paleoproterozoic shales and implications for reverse weathering on early Earth. Nat. Comms. 10, 2670.

Aubineau, J., El Albani, A., Chi Fru, E., Kipp, M.A., Ikouanga, J.N., Bekker, A., 2021. Benthic redox conditions and nutrient dynamics in the ca. 2.1 Ga Franceville sub-basin. Precambrian Res. 360, 106234.

Bankole, O.M., El Albani, A., Meunier, A., 2020. Elemental geochemistry and Nd isotope constraints on the basal siliciclastic succession of the middle Paleoproterozoic Francevillian Group, Gabon. Precambrian Res. 348, 105874.

Barbosa, J.S.F., Sabaté, P., 2004. Archean and Paleoproterozoic crust of the São Francisco Craton, Bahia, Brazil: geodynamic features. Precambrian Res. 133, 1–27.

Bau, M., Dulski, P., 1996. Distribution of yttrium and rare-earth elements in the Penge and Kuruman iron-formations, Transvaal Supergroup, South Africa. Precambrian Res. 79, 37–55.

Bau, M., Dulski, P., 1999. Comparing yttrium and rare earths in hydrothermal fluids from the Mid-Atlantic Ridge: implications for Y and REE behaviour during near-vent mixing and for the Y/Ho ratio of Proterozoic seawater. Chem. Geol. 155, 77–90.

Bauersachs, T., Schouten, S., Compaoré, J., Wollenzien, U., Stal, L.J., Sinninghe Damsteé, J.S., 2009. Nitrogen isotopic fractionation associated with growth on dinitrogen gas and nitrate by cyanobacteria. Limnol. Oceanogr. 54, 1403–1411.

Bebout, G.E., Fogel, M.L., 1992. Nitrogen-isotope compositions of metasedimentary rocks in the Catalina Schist, California: Implications for metamorphic devolatilization history. Geochim. Cosmo. Acta 56, 2839–2849.

Bender, M., Broecker, W., Gornitz, V., Middel, U., Kay, R., Sun, S.S., 1971. Geochemistry of three cores from the East Pacific Rise. Earth Planet. Sci. Lett. 12, 425–433.

Boström, K., 1970. Submarine volcanism as a source for iron. Earth Planet. Sci. Lett.. 9, 348–354.

Boström, K., Peterson, M.N.A., Joensuu, O., Fisher, D.E., 1969. Aluminum-poor ferromanganoan sediments on active oceanic ridges. J. Geophys. Res. 74, 3261–3270.

Boström, K., Joensuu, O., Valdes, S., Riera, M., 1972. Geochemical history of South Atlantic Ocean sediments since Late Cretaceous. Marine Geol. 12, 85–121.

Boström, K., Kraemer, T., Gartner, S., 1973. Provenance and accumulation rates of opaline silica, Al. Ti, Fe, Mn, Cu, Ni and Co in pacific pelagic sediments. Chem. Geol. 11, 123–148.

Bozdag, G.O., Libby, E., Pineau, R., Reinhard, C.T., RatCliff, W.C., 2021. Oxygen suppression of macroscopic multicellularity. Nat. Comm. 12, 2838.

Breuer, C., Pichler, T., 2013. Arsenic in marine hydrothermal fluids. Chem. Geol. 348, 2–14.

Brocks, J.J., Jarrett, A.J.M., Sirantoine, E., Hallmann, C., Hoshino, Y., Liyanage, T., 2017. The rise of algae in Cryogenian oceans and the emergence of animals. Nature 548, 578–581.

Bros, R., Stille, P., Gauthier-Lafaye, F., Weber, F., Clauer, N., 1992. Sm-Nd isotopic dating of Proterozoic clay material. Example from Francevillian sedimentary Series (Gabon). Earth Planet. Sci. Lett. 113, 207–218.

Buffield, N.J., 2009. Oxygen, animals and oceanic ventilation: an alternative view. Geobiology 7, 1–7.

Butterfield, N.J., 2015. Early evolution of the eukaryota. Palaeontology 58, 5–17.

Byrne, R.H., Sholkovitz, E.R., 1996. Marine chemistry and geochemistry of the lanthanides. In: Gschneidner, K.A., Eyring, L. (Eds.), Handbook on the Physics and Chemistry of Rare Earth Elements, vol 23. Elsevier Science B.V, pp. 497–593.

Calvert, S.E., Pedersen, S.T., 1996. Sedimentary geochemistry of manganese: Implications for the environment of formation of manganiferous black shale. Econ. Geol. 91, 36–47.

Canfield, D.E., Ngombi-Pemba, L., Hammarlund, E.U., Bengtson, S., Chaussidon, M., Gauthier-Lafaye, F., Meunier, A., Riboulleau, A., Rollion-Bard, C., Rouxel, O., Asael, A., Pierson-Wickmann, A.-C., El Albani, A., 2013. Oxygen dynamics in the aftermath of the Great Oxidation of Earth's atmosphere. Proc. Natl. Acad. Sci.U.S.A. 110, 16736–16741.

Capone, D.G., Hutchins, D.A., 2013. Microbial biogeochemistry of coastal upwelling regimes in a changing ocean. Nat. Geosci. 6, 711–717.

Carignan, J., Hild, P., Mevelle, G., Morel, J., Yeghicheyan, D., 2001. Routine analyses of trace elements in geological samples using flow injection and low pressure on-line liquid chromatography coupled to ICP-MS: a study of geochemical reference materials BR, DR-N, UB-N, An-G and GH. Geost. Newsletter 25, 187–198.

Chi Fru, E., Al Bahri, J., Brosson, C., Bankole, O., Aubineau, J., El Albani, A., Nederbragt, A., Oldroyd, A., Skelton, A., Lowhagen, L., Webster, D., Fantong, W.Y., Mills, B.J.W., Alcott, L.J., Konhauser, K.O., Lyons, T.W., 2023. Transient fertilization of a post-Sturtian Snowball ocean margin with dissolved phosphate by clay minerals. Nat. Comms. In Press.

Cole, D.B., Mills, D.B., Erwin, D.H., Sperling, E.A., Porter, S.M., Reinhard, C.T., Planavsky, N.J., 2020. On the co-evolution of surface oxygen levels and animals. Geobiology 18, 260–281.

Condie, K.C., 1993. Chemical composition and evolution of the upper continental crust: contrasting results from surface samples and shales. Chem. Geol. 104, 1–37.

Craig, J.M., Kumar, S., Hedges, S.B., 2023. The origin of eukaryotes and rise in complexity were synchronous with the rise in oxygen. Front. Bioinf. 3, 1233281.

Dalsgaard, T., Thamdrup, B., Canfield, D.E., 2005. Anaerobic ammonium oxidation (anammox) in the marine environment. Res. Microbiol. 156, 457–464.

Darnajoux, R., Magain, N., Renaudin, M., Zhang, X., 2019. Molybdenum threshold for ecosystem scale alternative vanadium nitrogenase activity in boreal forests. Proc. Natl. Acad. Sci. U.S.A. 116, 24682–24688.

Deassou Sezine, E., Soh Tamehe, L., Ganno, S., Nzepang Tankwa, M., Lemdjou, Y.B., Djomo, H.D., Nzenti, J.P., Bekker, A., 2022. Geochronological and geochemical constraints for the metavolcanosedimentary succession of the Nyong Complex, northwestern margin of the Congo craton: Implications for depositional age and tectonic setting of associated banded iron formations. Precambrian Res. 383, 106910.

Delvigne, C., Cardinal, D., Hofmann, A., André, L., 2012. Stratigraphic changes of Ge/Si, REE+Y and silicon isotopes as insights into the deposition of a Mesoarchaean banded iron formation. Earth Planet. Sci. Lett. 355–356, 109–118.

Dennen, K.O., Johnson, C.A., Otter, M.L., Silva, S.R., Wandless, G.A., 2006. δ^{15}N and non-carbonate δ^{13}C values for two petroleum source rock reference materials and a marine sediment reference material. U. S. Geological Survey Open File Report 2006-1071.

Dodd, M.S., Shi, W., Li, C., Zhang, Z., Cheng, M., Gu, H., Hardisty, D.S., Loyd, S.J., Wallace, M.W., Hood, A.S., Lamothe, K.L., Mills, B.J.W., Poulton, S.W., Lyons, T.W., 2023. Uncovering the Ediacaran phosphorus cycle. Nature in Press. https://doi.org/10.1038/s41586-023-06077-6.

Dong, Z.G., Robbins, L.J., Konhauser, K.O., Zhang, B.-L., Zhang, L.-C., Li, J., Li, W.-J., Zhang, L., Wang, C.-L., 2023a. Episodic ventilation of euxinic bottom waters triggers the formation of black shale-hosted Mn carbonate deposits. Geochim. Cosmochim. Acta 341, 132–149.

Dong, F., Yin, L., Dong, Z., Liu, J., Tan, Z., Long, X., Jia, W., Li, J., 2023b. Dynamic deep-water oxygenation of marginal seas in the aftermath of the Sturtian Snowball Earth: Insights from redox-hydrological reconstructions of the Nanhua basin (South China). Precambrian Res. 398, 107219.

dos Santos, F.H., da Silver Amaral, W., Martins, D.T., de Souza, A.C.B., 2023. Zircon U-Pb geochronology of manganese-rich rocks from the Borborema Province, Northeast Brazil: adding a new piece to the global inventory of Paleoproterozoic manganese mineralization. Min. Dep. 58, 531–551.

Dupont, C., Butcher, A., Valas, R., Bourne, P., Caetano-Anollés, G., 2010. History of biological metal utilization inferred through phylogenomic analysis of protein structures. Proc. Natl. Acad. Sci. U.S.A. 107, 10567.

Dupont, C.L., Yang, S., Palenik, B., Bourne, P.E., 2006. Modern proteomes contain putative imprints of ancient shifts in trace metal geochemistry. Proc. Natl. Acad. Sci. U.S.A. 103, 17822–17827.

Eckford-Soper, L.K., Andersen, K.H., Hansen, T.F., Canfield, D.E., 2022. A case for an active eukaryotic marine biosphere during the Proterozoic era. Proc. Natl. Acad. Sci. U.S.A. 119 (41), e2122042119.

El Albani, A., Bengtson, S., Canfield, D.E., Bekker, A., Macchiarelli, R., Mazurier, A., Hammarlund, E.U., Boulvais, P., Dupuy, J.-J., Fontaine, C., Fürsich, F.T., Gauthier-Lafaye, F., Janvier, P., Javaux, E., Ossa Ossa, F., Pierson-Wickmann, A.-C., Riboulleau, A., Sardini, P., Vachard, D., Whitehouse, M., Meunier, A., 2010. Large colonial organisms with coordinated growth in oxygenated environments 2.1 Gyr ago. Nature 466, 100–104.

El Albani, A., Bengtson, S., Canfield, D.E., Riboulleau, A., Bard, C.R., Macchiarelli, R., Pemba, L.N., Hammarlund, E., Meunier, A., Mouele, I.M., Benzerara, K., Bernard, S., Boulvais, P., Chaussidon, M., Cesari, C., Fontaine, C., Chi Fru, E., Ruiz, J.M.G., Gauthier-Lafaye, F., Mazurier, A., Pierson-Wickmann, A.C., Rouxel, O., Trentesaux, A., Vecoli, M., Versteegh, G.J.M., White, L., Whitehouse, M., Bekker, A., 2014. The 2.1 Ga old Francevillian biota: biogenicity, taphonomy and biodiversity. PLoS One 9, e99438.

El Albani, A., Konhauser, K.O., Somogyi, A., Ikouanga, J.N., Lamboux, A., Bichert, J., Chi Fru, E., Fontaine, C., Mazurier, A., Riboulleau, A., Wickmann, P.-A.-C., Albarède, F., 2023. A search for life in Palaeoproterozoic marine sediments using Zn isotopes and geochemistry. Earth Planet. Sci Lett. 612, 118169.

El Albani, A., Mangano, M.G., Buatois, L.A., Bengtson, S., Riboulleau, A., Bekker, A., Konhauser, K., Lyons, T., Rollion-Bard, C., Bankole, O., Lekele Baghekema, S.G., Meunier, A., Trentesaux, A., Mazurier, A., Aubineau, J., Laforest, C., Fontaine, C., Recourt, P., Chi Fru, E., Macchiarelli, R., Reynaud, J.Y., Gauthier-Lafaye, F., Canfield, D.E., 2019. Organism motility in an oxygenated shallow-marine environment 2.1 billion years ago. Proc. Natl Acad. Sci. USA 116, 3431–3436.

Erwin, D.H., Laflamme, M., Tweedt, S.M., Sperling, E.A., Pisani, D., Peterson, K.J., 2011. The Cambrian Conundrum: Early divergence and later ecological success in the early history of animals. Science 334, 1091–1097.

Fakhraee, M., Tarhan, L.G., Reinhard, C.T., Crowe, S.A., Lyons, T.W., Planavsky, N., 2023. Earth's surface oxygenation and the rise of eukaryotic life: Relationships to the Lomagundi positive carbon isotope excursion revisited. Earth-Sci. Rev., 104398

Fedo, C.M., Babechuk, M.G., 2023. Petrogenesis of siliciclastic sediments and sedimentary rocks explored in three-dimensional Al_2O_3–CaO*+Na_2O–K_2O–FeO+MgO (A–CN–K–FM) compositional space. Can. J. Earth Sci. 60, 818–838.

Fedo, C.M., Nesbitt, H.W., Young, G.M., 1995. Unraveling the effects of potassium metasomatism in sedimentary rocks and paleosols, with implications for paleoweathering conditions and provenance. Geology 23, 921–924.

Feely, R.A., Trefry, J.H., Lebon, G.T., German, C.R., 1998. The relationship between P/Fe and V/Fe ratios in hydrothermal precipitates and dissolved phosphate in seawater. Geophys. Res. Lett. 25, 2253–2256.

Feybesse, J.L., Johan, V., Triboulet, C., Guerrot, C., Mayaga-Mikolo, F., Bouchot, V., Eko N'dong, J., 1998. The West Central African Belt; a model of 2.5-2.0 Ga accretion and two-phase orogenic evolution. Precambr. Res. 87, 161–216.

Fischer, W.W., Hemp, J., Johnson, J.E., 2015. Manganese and the evolution of photosynthesis. Orig. Life Evol. Biosph.ys. 45, 351–357.

Gauthier-Lafaye, F., Weber, F., 2003. Natural nuclear fission reactors: time constraints for occurrence, and their relation to uranium and manganese deposits and to the evolution of the atmosphere. Precambrian Res. 120, 81–100.

Guilbaud, R., Poulton, S.W., Thompson, J., Husband, K.F., Zhu, M., Zhou, Y., Shields, G. A., Lenton, T.M., 2020. Phosphorus-limited conditions in the early Neoproterozoic Ocean maintained low levels of atmospheric oxygen. Nat. Geosci. 13, 296–301.

Hein, J.R., Koschinsky, A., Halbach, P., Manheim, F.T., Bau, M., Kang, J.-K., Lubick, N., 1997. Iron and manganese oxide mineralization in the Pacific. Geochem. Soc. Spec. Publ. 119, 123–138.

Hernandez, J.A., Curatti, L., Azar, C.P., Rubio, L.M., 2008. Metal trafficking for nitrogen fixation: NifQ donates molybdenum to NifEN/NifH for the biosynthesis of the nitrogenase FeMo-cofactor. Proc. Natl. Acad. Sci. U.S.A. 105, 11679–11684.

Huang, Q., Pi, D.H., Jiang, S.Y., Liu, D., Yan, H., Mänd, K., Kirsimäe, K., Bishop, B., Robbins, L.J., Yang, S.S., 2022. The dual role of microbes in the formation of the Malkantu manganese carbonate deposit, NW China: Petrographic, geochemical, and experimental evidence. Chem. Geol. 606, 120992.

Ikouanga, J.N., Fontaine, C., Bourdelle, F., Elmola, A.A., Bankole, O.M., Reisberg, L., Pierson-Wickmann, A.-C., Riboulleau, A., Trentesaux, A., Laforest, C., Meunier, A., El Albani, A., 2023. Taphonomy of early life (2.1 Ga) in the Francevillian basin (Gabon): Role of organic mineral interactions. Precambrian Res. 395, 107155.

Ingall, E.D., Van Cappellen, P., 1990. Relation between sedimentation rate and burial of organic phosphorus and organic carbon in marine sediments. Geochim. Cosmo. Act 54, 373–386.

Javaux, E. 2011. Early eukaryotes in Precambrian oceans. In: Origins and Evolution of Life: An Astrobiological Perspective, M. Gargaud, P.Lopez-Garcia, H. Martin, Eds. Cambridge University Press, Cambridge, United Kingdom, chap. 26, pp. 414–449.

Jelen, B.I., Giovannelli, D., Falkowski, P.G., 2016. The role of microbial electron transfer in the coevolution of the biosphere and geosphere. Annu. Rev. Microbiol. 70, 45–62.

Jian, X., Guan, P., Zhang, W., Feng, F., 2013. Geochemistry of Mesozoic and Cenozoic sediments in the northern Qaidam basin, northeastern Tibetan Plateau: implications for provenance and weathering. Chem. Geol. 360–361, 74–88.

Jiang, C.Z., Halevy, I., Tosca, N.J., 2022. Kinetic isotope effect in siderite growth: Implications for the origin of banded iron formation siderite. Geochim. Cosmochim. Acta 322, 260–273.

Kellogg, R.M., McIlvin, M.R., Vedamati, J., Twinning, B.S., Moffett, J.W., Marchetti, A., Moran, D.M., Saito, M.A., 2020. Efficient zinc/cobalt inter-replacement in northeast Pacific diatoms and relationship to high surface dissolved Co: Zn ratios. Limnol. Oceanogr. 65, 2557–2582.

Kellogg, R.M., Moosburner, M.A., Cohen, N.R., Hawco, N.J., McIlvin, M.R., Moran, D.M., DiTullio, G.R., Subhas, A.V., Allen, A.E., Saito, M.A., 2022. Adaptive responses of marine diatoms to zinc scarcity and ecological implications. Nat. Commun. 13, 1995.

Kipp, M.A., Stüeken, E.E., Yun, M., Bekker, A., Buick, R., 2018. Pervasive aerobic nitrogen cycling in the surface ocean across the Paleoproterozoic Era. Earth Planet. Sci. Lett. 500, 117–126.

Klinkhammer, G., Elderfield, H., Hudson, A., 1983. Rare earth elements in seawater near hydrothermal vents. Nature 305, 185–188.

Knoll, A.H., Javaux, E.J., Hewitt, D., Cohen, P., 2006. Eukaryotic organisms in Proterozoic oceans. Philos. Trans. R. Soc. Lond. B Biol. Sci. 361, 1023–1038.

Kuhn, T., Bau, M., Blum, N., Halbach, P., 1998. Origin of negative Ce anomalies in mixed hydrothermal–hydrogenetic Fe–Mn crusts from the Central Indian Ridge. Earth Planet. Sci. Lett. 163, 207–220.

Kump, L.R., Junium, C., Arthur, M.A., Brasier, A., Fallick, A., Melezhik, V., Lepland, A., CČrne, A.E., Luo, G., 2011. Isotopic evidence for massive oxidation of organic matter following the great oxidation event. Science 334, 1694–1696.

Laakso, T.A., Sperling, E.A., Johnston, D.T., Knoll, A.H., 2020. Ediacaran reorganization of the marine phosphorus cycle. Proc. Natl. Acad. Sci. U.S.A. 117, 11961–11967.

Marty, B., Zimmermann, L., Pujol, M., Burgess, R., Philippot, P., 2013. Nitrogen isotopic composition and density of the Archean atmosphere. Science 342, 101–104.

Mayika, K.B., Moussavou, M., Prave, A.R., Lepland, A., Mbina, M., Kirsimäe, K., 2020. The Paleoproterozoic Francevillian succession of Gabon and the Lomagundi-Jatuli event. Geology 48, 1101–1104.

McLennan, S.M., Hemming, S., McDaniel, D.K., Hanson, G.N., 1993. Geochemical approaches to sedimentation, provenance, and tectonics. Geol. Soc. Am. Spec. Paper 21–40.

Mhlanga, X.R., Tsikos, H., Lee, B., Rouxel, J.O., Boyce, A.C., Harris, C., Lyons, T.W., 2023. The Palaeoproterozoic Hotazel BIF-Mn Formation as an archive of Earth's earliest oxygenation. Earth Sci. Rev. 240, 104389.

Mills, D.B., Ward, L.M., Jones, C. Canfield D.E., 2014. Oxygen requirements of the earliest animals. Proc. Natl. Sci. U.S.A. 111, 4168–4172.

Moore, D.M., Reynolds, R.C., Jr., 1997. *X-Ray Diffraction and the Identification and Analysis of Clay Minerals*, 2nd ed. xviii + 378 pp. Oxford, New York: Oxford University Press.

Moore, E.K., Jelen, B.I., Giovannelli, D., Raanan, H., Falkowski, P.G., 2017. Metal availability and the expanding network of microbial metabolisms in the Archaean eon. Nat. Geosci. 10, 629–636.

Mossmann, D.J., Gauthier-Lafaye, F., Jackson, S.E., 2005. Black shales, organic matter, ore genesis and hydrocarbon generation in the Paleoproterozoic Franceville series, Gabon. Precambrian Res. 137, 253–272.

Ngombi Pemba, L., El Albani, A., Meunier, A., Grauby, O., Gauthier-Lafaye, F. 2014. From detrital heritage to diagenetic transformations, the message of clay minerals contained within shales of the Palaeoproterozoic Francevillian basin (Gabon). Precambrian Res. 255, 63–76.

Ossa Ossa, F., Eickmann, B., Hofmann, A., Planavsky, N.J., Asael, D., Pambo, F., Bekker, A., 2018. Two-step deoxygenation at the end of the Paleoproterozoic Lomagundi Event. Earth Planet. Sci. Lett. 486, 70–83.

Ossa Ossa, F., Spangenberg, J.E., Bekker, A., König, S., Stüeken, E.E., Hofmann, A., Poulton, S.W., Yierpan, A., Varas-Reus, M.I., Eickmann, B., Andersen, M.B., Schoenberg, R., 2022. Moderate levels of oxygenation during the late stage of Earth's Great Oxidation Event. Earth Planet. Sci. Lett. 594, 117716.

Ossa Ossa, F., Pons, M.-L., Bekker, A., Hofmann, A., Poulton, S.W., Andersen, M.B., Agangi, A., Gregory, D., Reinke, C., Steinhilber, B., Marin-Carbonne, J., Schoenberg, R., 2023. Zinc enrichment and isotopic fractionation in a marine habitat of the c. 2.1 Ga Francevillian Group: A signature of zinc utilization by eukaryotes? Earth Planet. Sci. Lett 611, 118147.

Pambo, F., Guiraud, M., Quesne, D., Gauthier-Lafaye, F., Azzibrouck, G., Lang, J., 2006. The Proterozoic Franceville Basin (S.E. Gabon); an example of interaction between marine sedimentation and extensional faulting. Afr. Geosci. Rev. 13, 77–106.

Pecoits, E., Gingras, M.K., Barley, M.E., Kappler, A., Posth, N.R., Konhauser, K.O., 2009. Petrography and geochemistry of the Dales Gorge banded iron formation: Paragenetic sequence, source and implications for palaeo-ocean chemistry. Precambrian Res. 172, 163–187.

Planavsky, N., Bekker, A., Rouxel, O.J., Kamber, B., Hofmann, A., Knudsen, A., Lyons, T. W., 2010. Rare Earth Element and yttrium compositions of Archean and Paleoproterozoic Fe formations revisited: New perspectives on the significance and mechanisms of deposition. Geochim. Cosmo. Acta 74, 6387–6405.

Planavsky, N.J., Reinhard, C.T., Wang, X., Thomson, D., McGoldrick, P., Rainbird, R.H., Johnson, T., Fischer, W.W., Lyons, T.W., 2014. Low mid-Proterozoic atmospheric oxygen levels and the delayed rise of animals. Science 346, 635–638.

Poulton, S.W., Canfield, D.E., 2005. Development of a sequential extraction procedure for iron: Implications for iron partitioning in continentally derived particulates. Chem. Geol. 214, 209–221.

Poulton, S.W., Bekker, A., Cumming, V.M., Canfield, D.E., Johnston, D.T., 2021. A 200-million-year delay in permanent atmospheric oxygenation. Nature 592, 232–236.

Raiswell, R., Hardisty, D.S., Lyons, T.M., Canfield, D.E., Owens, J.D., Planavsky, N.J., Poulton, S.W., Reinhard, C.T., 2018. The iron paleoredox proxies: A guide to the pitfalls, problems and proper practice. Am. J. Sci. 318, 491–526.

Rasmussen, B., Muhling, J.R., Suvorova, A., Fischer, W.W., 2021. Apatite nanoparticles in 3.46–2.46 Ga iron formations: Evidence for phosphorus-rich hydrothermal plumes on early Earth. Geology 49, 647–651.

Redfield, A.C., 1958. The biological control of chemical factors in the environment. Am. Sci. 46 (230A), 205–221.

Reinhard, C.T., Planavsky, N.J., Olson, S.L., Erwin, D.H., 2016. Earth's oxygen cycle and the evolution of animal life. Proc. Natl. Acad. Sci. U.S.A. 113, 8933–8938.

Reinhard, C.T., Planavsky, N.J., Gill, B.C., Ozaki, K., Robbins, L.J., Lyons, T.W., Fischer, W.W., Wang, C., Cole, D.B., Konhauser, K.O., 2017. Evolution of the global phosphorus cycle. Nature 541, 386–389.

Reinhard, C.T., Planavsky, N.J., Ward, B.A., Love, G.D., Le Hir, G., Ridgwell, A., 2020. The impact of marine nutrient abundance on early eukaryotic ecosystems. Geobiology 18, 139–151.

Reynaud, J.Y., Trentesaux, A., El Albani, A., Aubineau, J., Ngombi-Pemba, L., Guiyeligou, G., Bouton, P., Gauthier-Lafaye, F., Weber, F., 2018. Depositional setting of the 2.1 Ga Francevillian macrobiota (Gabon): Rapid mud settling in a shallow basin swept by high-density sand flows. Sedimentology 65, 670–701.

Robbins, L.J., Lalonde, S.V., Saito, M.A., Planavsky, N.J., Mloszewska, A.M., Pecoits, E., Scott, C., Dupont, C.L., Kappler, A., Konhauser, K.O., 2013. Authigenic iron oxide proxies for marine zinc over geological time and implications for eukaryotic metallome evolution. Geobiology 11, 295–306.

Roy, S., 1992. Environments and processes of manganese deposition. Econ. Geol. 87, 218–1236.

Ruttenberg, K.C., 2003. The global phosphorus cycle. Treat. Geochem. 8, 585–643.

Ruttenberg, K., Berner, R.A., 1993. Authigenic apatite formation and burial in sediments from non-upwelling, continental margin environments. Geochim. Cosmochim. Acta 57, 991–1007.

Saito, M.A., Sigman, D., Morel, F., 2003. The bioinorganic chemistry of the ancient ocean: the co-evolution of cyanobacterial metal requirements and biogeochemical cycles at the Archean-Proterozoic boundary? Inorg. Chim. Acta 356, 308–318.

Sano, Y., Pillinger, C.T., 1990. Nitrogen isotopes and N_2/Ar ratios in chests: An attempt to measure time evolution of atmospheric 6^{15}N value. Geochem. J. 24, 315–325.

Sanz-Montero, M., del Buey, P., Cabestreto, Ó., Sánchez-Román, M., 2023. Isotopic signatures of microbial Mg-carbonates deposited in an ephemeral hyperalkaline lake (Central Spain): Paleoenvironmental implications. Minerals 13, 617.

Sawaki, Y., Moussavou, M., Sato, T., Suzuki, K., Ligna, C., Asanuma, H., Sakata, S., Obayashi, H., Hirata, T., 2017. Chronological constraints on the Paleoproterozoic Francevillian Group in Gabon. Geosci. Front. 8, 397e407.

Scott, C., Planavsky, N.J., Dupont, C.L., Kendall, B., Gill, B.C., Robbins, L.J., Husband, K. F., Arnold, G.L., Wing, B.A., Poulton, S.W., Bekker, A., Anbar, A.D., Konhauser, K.O., Lyons, T.W., 2013. Bioavailability of zinc in marine systems through time. Nat. Geosci. 6, 125.

Sharoni, S., Halevy, I., 2022. Rates of seafloor and continental weathering govern Phanerozoic marine phosphate levels. Nat. Geosci. 16, 75–81.

Sigman, D.M., Karsh, K.L., Casciotti, K.L., 2009. Ocean process tracers: Nitrogen isotopes in the ocean. In: Steele, J.H., Turekian, K., Thorpe, S. (Eds.), Encyclopedia of Ocean Sciences. Academic, London, pp. 40–54.

Soh Tamehe, L., Wei, C.T., Ganno, S., Rosière, C.A., Nzenti, J.P., Gatse Ebotehouna, C., Lu, G.W., 2021. Depositional age and tectonic environment of the Gouap banded iron formations from the Nyong Group, SW Cameroon: Insights from isotopic, geochemical and geochronological studies of drillcore samples. Geosci. Front. 12, 549–572.

Soh Tamehe, L., Wei, C.T., Ganno, S., Rosière, C.A., Li, H., Brando Soares, M., Nzenti, J. P., Santos, J.O.S., Bekker, A., 2022. Provenance of metasiliciclastic rocks at the East Gabonian Block: Implications for deposition of BIFs and crustal evolution in southwestern Cameroon. Precambrian Res. 376, 106677.

Sperling, E.A., Halverson, G.P., Knoll, A.H., Macdonald, F.A., Johnston, D.T., 2013. A basin redox transect at the dawn of animal life. Earth Planet. Sci. Lett. 371–372, 143–155.

Stüeken, E.E., 2013. A test of the nitrogen-limitation hypothesis for retarded eukaryote radiation: Nitrogen isotopes across a Mesoproterozoic basinal profile. Geochim. Cosmochim. Acta 120, 121–139.

Stüeken, E.E., Kipp, M.A., Koehler, M.C., Buick, R., 2016. The evolution of Earth's biogeochemical nitrogen cycle. Earth Sci. Rev. 160, 220–239.

Stüeken, E.E., Zaloumis, J., Meixnerová, J., Buick, R., 2017. Differential metamorphic effects on nitrogen isotopes in kerogen extracts and bulk rocks. Geochim. Cosmochim. Acta 217, 80–94.

Syverson, D.D., Reinhard, C.T., Isson, T.T., Holstege, C.J., Katchinoff, J.A.R., Tutolo, B. M., Etschmann, B., Brugger, J., Planavsky, N.J., 2021. Nutrient supply to planetary biospheres from anoxic weathering of mafic oceanic crust. Geophy. Res. Lett. 48, e2021GL094442.

Taylor, S.R., McLennan, S.M., 1985. The continental crust: Its composition and evolution. U.S. Department of Energy Office of Scientific and Technical Information, United States. OSTI Identifier 6582885.

Teixeira, W., Oliveira, E.P., Peng, P., Dantas, E.L., Hollanda, M.H.B.M., 2017. U-Pb geochronology of the 2.0 Ga Itapecerica graphite-rich supracrustal succession in the São Francisco Craton: Tectonic matches with the North China Craton and paleogeographic inferences. Precambrian Res. 293, 91–111.

Thiéblemont, D., Castaing, C., Billa, M., Bouton, P., Préat, A., 2009. Notice explicative de la carte géologique et des ressources minérales de la République gabonaise à 1/1,000,000.

Timmermans, K.R., Snoek, J., Gerringa, L.J.A., Zondervan, I., de Baar, H.J.W., 2001. Not all eukaryotic algae can replace zinc with cobalt: *Chaetoceros calcitrans* (Bacillariophyceae) versus *Emiliania huxleyi* (Prymnesiophyceae). Limnol. Oceanogr. 46 (3), 699–703.

Tribovillard, N., Algeo, T.J., Lyons, T., Riboulleau, A., 2006. Trace metals as paleoredox and paleoproductivity proxies: An update. Chem. Geol. 232, 12–32.

Tyrrell, T., 1999. The relative influences of nitrogen and phosphorus on oceanic primary production. Nature 400, 525–531.

Van Maldegem, L.M., Sanjofre, P., Weijers, J.W.H., Wolkenstein, K., Strother, P.K., Wörmer, L., Hefter, J., Nettersheim, B.J., Hoshino, Y., Schouten, S., Damsté, J.S.S., Nath, N., Griesinger, C., Kuznetsov, N.B., Elie, M., Elvert, M., Tegelaar, E., Gleixner, G., Hallmann, C., 2019. Bisnorgammacerane traces predatory pressure and the persistent rise of algal ecosystems after Snowball Earth. Nat 10, 476.

Vuillemin, A., Mayr, C., Schuessler, J.A., Friese, A., Bauer, K.W., Lücke, A., Heuer, V.B., Glombitza, C., Henny, C., von Blanckenburg, F., Russell, J.M., Bijaksana, S., Vogel, H., Crowe, S.A., Kallmeyer, J., 2023. A one-million-year isotope record from siderites formed in modern ferruginous sediments. GSA Bull. 135, 504–522.

Wang, Z., Wang, X., Shi, X., Tang, D., Stüeken, E.E., Song, H., 2020. Coupled Nitrate and Phosphate Availability Facilitated the Expansion of Eukaryotic Life at Circa 1.56 Ga. JGR Biogeosci. 125, 4. e2019JG005487.

Wang, X., Zhang, S., Ye, Y., Ma, S., Su, J., Wang, H., Canfield, D.E. 2023. Nitrogen cycling during the Mesoproterozoic as informed by the 1400 million year old Xiamaling Formation. Earth-Sci Rev. 243, 104499.

Ward, B.A., Dutkiewicz, S., Jahn, O., Follows, M.J., 2012. A size-structured food-web model for the global ocean. Limnol. Oceanogr. 57, 1877–1891.

Weber, F., 1968. Une série précambrienne du Gabon, le Francevillian sédimentologie, géochimie, relations avec les gîtes minéraux associés. Université de Strasbourg, Strasbourg, p. 328.

Weber, F., Gauthier-Lafaye, F., 2013. No proof from carbon isotopes in the Francevillian (Gabon) and Onega (Fennoscandian shield) basins of a global oxidation event at 1980–2090 Ma following the Great Oxidation Event (GOE). C. R. Geosci. 345, 28–35.

Wheat, C.G., Feely, R.A., Mottl, M.J., 1996. Phosphate removal by oceanic hydrothermal processes: An update of the phosphorus budget in the oceans. Geochim. Cosmochim. Acta 60, 3593–3608.

Wheat, C.G., Fisher, A.T., 2008. Massive, low-temperature hydrothermal flow from a basaltic outcrop on 23 Ma seafloor of the Cocos Plate: chemical constraints and implications. Geochem. Geophys. Geosyst. 9, Q12014.

Wheat, C.G., McManus, J., Mottl, M.J., Giambalvo, E., 2003. Oceanic phosphorus imbalance: Magnitude of the mid-ocean ridge flank hydrothermal sink. Geophy. Res. Lett. 30, 1895–1899.

Williams, L.B., Ferrell Jr, R.E., Hutcheon, I., Bakel, A.J., Walsh, M.M., Krouse, H.R., 1995. Nitrogen isotope geochemistry of organic matter and minerals during diagenesis and hydrocarbon migration. Geochim. Cosmochim. Acta 59, 765–779.

Wittkop, C., Swanner, E.D., Grengs, A., Lambrecht, N., Fakhraee, M., Myrbo, A., Bray, A. W., Poulton, S.W., Katsev, S., 2020. Evaluating a primary carbonate pathway for manganese enrichments in reducing environments. Earth Plant. Sci. Lett. 538, 116201.

Yoshida, S., Mayika, K.B., Ishihara, Y., Moussavou, M., Asanuma, H., Sato, T., Hirata, T., Ligna, C., Sawaki, Y., Edou-Minko, A., 2023. Depositional condition of Paleoproterozoic Francevillian carbonate rocks re- visited from rare earth element contents. Geosci. Front., 101771. In Press.

Zhang, L., Horita, J., Cole, D.R., Zhou, J., Lovley, D.R., Phelps, T.J., 2001. Temperature-dependent oxygen and carbon isotope fractionations of biogenic siderite. Geochem. Cosmochim. Acta 65, 2257–2271.

Zhang, X., Sigman, D.M., Morel, F.M.M., Kraepiel, A.M.L., 2014. Nitrogen isotope fractionation by alternative nitrogenases and past ocean anoxia. Proc. Natl. Acad. Sci. 111, 4782–4787.

Zhu, S., Zhu, M., Knoll, A.H., Yin, Z., Zhao, F., Sun, S., Qu, Y., Shi, M., Liu, H., 2016. Decimetre-scale multicellular eukaryotes from the 1.56-billion-year-old Gaoyuzhuang Formation in North China. Nat. Commun. 7, 11500.